Universidade de Aveiro Departamento de Engenharia Mecânica
2020

Pedro Mendes Costa

Modelling and structural analysis based on numerical simulation of a car chassis

Modelação e análise estrutural com base em simulação numérica de um chassis automóvel

This work was supported by projects UIDB/00481/2020 and UIDP/00481/2020 (Fundação para a Ciência e a Tecnologia, FCT); and CENTRO-01-0145-FEDER-022083 (Centro Portugal Regional Operational Programme, Centro2020), under the PORTUGAL 2020 Partnership Agreement through the European Regional Development Fund.

Universidade de Aveiro Departamento de Engenharia Mecânica
2020

Pedro Mendes Costa

Modelling and structural analysis based on numerical simulation of a car chassis

Modelação e análise estrutural com base em simulação numérica de um chassis automóvel

Dissertação apresentada à Universidade de Aveiro para cumprimento dos requisitos necessários à obtenção do grau de Mestre em Engenharia Mecânica, realizada sob orientação de Robertt Angelo Fontes Valente, Professor Associado, Departamento de Engenharia Mecânica, Universidade de Aveiro.

o júri / the jury

presidente / president

Prof. Doutor João Alexandre Dias de Oliveira
Professor Auxiliar, Departamento de Engenharia Mecânica, Universidade de Aveiro

Prof. Doutor Marco Paulo Lages Parente
Professor Auxiliar, Departamento de Engenharia Mecânica, Faculdade de Engenharia da Universidade do Porto

Prof. Doutor Robertt Angelo Fontes Valente
Professor Associado, Departamento de Engenharia Mecânica, Universidade de Aveiro (orientador)

agradecimentos / acknowledgements

Gostaria de expressar o meu agradecimento aos vários professores que surgiram ao longo de toda a minha formação, por todos os ensinamentos que me foram transmitidos.

Gostaria também de endereçar os meus sinceros agradecimentos ao meu orientador, o Professor Doutor Robertt Valente, por ter investido parte do seu precioso tempo para me dar apoio, pelo rigor exigido e pelas suas valiosas e construtivas sugestões.

Uma palavra de apreço também a todos os meus colegas da *Engenius - UA Formula Student*, pelos desafios por que passámos e por todo o conhecimento que me foi transmitido. Um agradecimento também ao *faculty advisor* da equipa, o Professor Doutor João Oliveira, pela sua paciência, por todas as discussões enriquecedoras e pelo apoio dado ao projeto.

Em último lugar, estou imensamente grato à minha família, em especial aos meus pais e irmãos, por todo o suporte e encorajamento, que me ajudou a chegar até aqui. Uma nota especial ao meu irmão André, pela sua preciosa ajuda na revisão da escrita deste documento. Quaisquer erros que tenham escapado são da minha total responsabilidade.

keywords Formula Student, Vehicle chassis, Numeric simulation, Structural analysis, Composite space frame.

abstract The development of a Formula Student chassis must be done with the aid of numerical simulations and structural analyses, in order to ensure a light, safe solution, with good torsional stiffness. The aim of this work was to study several existing solutions, identifying the strengths and weaknesses of each one of these, with the ultimate goal of proposing an improved solution. Loading scenarios to which a chassis may be subjected were analysed, and there was a brief search on the most suited materials. As a means to compare the different solutions, the most important criteria to be considered were defined, and torsional and both frontal and lateral impact simulations were conducted. The resulting chassis consists of a carbon composite space frame, which showed significant improvements regarding torsional stiffness and impact response when compared with the already existing solutions.

palavras-chave Formula Student, Chassis automóvel, Simulação numérica, Análise estrutural, Chassis tubular compósito.

resumo O desenvolvimento de um chassis de Formula Student deve ser feito com recurso a simulações numéricas e análises estruturais, de forma a garantir uma solução leve, com boa rigidez à torção, e segura. O objetivo deste trabalho passou por estudar diferentes soluções já existentes, identificando os pontos fortes e fracos de cada uma, com o objetivo último de propor uma solução melhorada. Foram estudados os diferentes carregamentos a que um chassis automóvel pode estar sujeito, e foi feita uma breve pesquisa dos materiais mais adequados. De forma a comparar as diferentes soluções já existentes, definiram-se os critérios mais importantes a ter em conta, e foram realizadas simulações à torção, assim como simulações de impacto frontal e lateral. O chassis desenvolvido consiste num chassis tubular com tubos de carbono, e apresentou melhorias significativas em termos de rigidez torsional e de resposta a impactos quando comparado com as soluções já existentes estudadas.

Contents

I Introduction and background **3**

1 Introduction **5**
1.1 Formula Student competition 5
1.2 Problem definition and objectives 5
1.3 Reading guide 6

2 Theoretical foundations **7**
2.1 Introduction 7
2.2 Chassis types 7
2.2.1 Twin-tube or ladder frame chassis 7
2.2.2 Space frame chassis 7
2.2.3 Monocoque chassis 8
2.2.4 Hybrid chassis 8
2.2.5 Composite space frame chassis 9
2.3 Vehicle loading 10
2.3.1 Vertical bending case 10
2.3.2 Lateral bending case 11
2.3.3 Horizontal lozenging 12
2.3.4 Longitudinal torsion 12
2.3.5 Crash cases 13
2.4 Torsional stiffness 13
2.4.1 Torsional stiffness determination 13
2.4.2 Torsional stiffness target 14
2.5 Loads in the wheels 17
2.6 Chassis components 17
2.7 Ergonomics 17
2.8 Materials 18
2.8.1 Material selection 18
2.8.2 Composite materials 20
2.8.2.1 Fibres 21
2.8.2.2 Matrix 22
2.8.3 Space frame chassis 23
2.8.3.1 Metal tube 23
2.8.3.2 Carbon fibre composite tube 24
2.8.4 Monocoque chassis 26

II Comparison and analysis of different types of chassis 27

3 Introduction and general procedures 29
3.1 Parameters of evaluation . . . 29
3.2 Finite element analysis tests . . . 30
3.2.1 Torsional stiffness simulation . . . 30
3.2.2 Driver safety . . . 30
3.2.2.1 Frontal impact simulation . . . 31
3.2.2.2 Lateral impact simulation . . . 31
3.3 Simulations setup . . . 32

4 Finite element analysis 33
4.1 Steel space frame with beam elements . . . 33
4.1.1 Model definition . . . 33
4.1.2 Results . . . 34
4.1.2.1 Torsional stiffness . . . 34
4.1.2.2 Frontal impact . . . 36
4.1.2.3 Lateral impact . . . 38
4.2 Steel space frame with shell elements . . . 39
4.2.1 Results . . . 40
4.2.1.1 Torsional stiffness . . . 40
4.2.1.2 Frontal impact . . . 42
4.2.1.3 Lateral impact . . . 43
4.3 Composite space frame . . . 44
4.3.1 Materials and profiles . . . 44
4.3.2 Mesh . . . 45
4.3.3 Results . . . 45
4.3.3.1 Torsional stiffness . . . 45
4.3.3.2 Frontal impact . . . 47
4.3.3.3 Lateral impact . . . 48
4.4 Monocoque chassis . . . 49
4.4.1 Materials and profiles . . . 49
4.4.2 Mesh . . . 49
4.4.3 Results . . . 52
4.4.3.1 Torsional stiffness . . . 52
4.4.3.2 Frontal impact . . . 54
4.4.3.3 Lateral impact . . . 55

5 Model comparison 57

III Final solution 59

6 Development of the new solution 61
6.1 Chassis improvement . . . 61
6.2 Design process . . . 62

6.3 Assessment of the positioning of the additional tubes 62
6.3.1 Results 63
6.4 Selection of the profiles 63
6.5 First iteration analysis 65
6.5.1 Torsional stiffness 65
6.5.2 Impact simulations 66

7 Analysis of the final design **67**
7.1 Final design 67
7.2 Torsional stiffness 68
7.3 Frontal impact 70
7.4 Lateral impact 71

8 Conclusions and recommendations **73**

References **78**

Appendices **79**

A Formula Student templates **79**

B Concept scoring details **81**
B.1 Driver safety 81
B.2 Ease of manufacture 82
B.3 Cost estimation 83

Intentionally blank page.

List of Tables

2.1 Loads on the front wheel, for different driving scenarios. 17
2.2 Performance indexes of potential materials. 20
2.3 Minimum material requirements for steel tubes [1]. 23
2.4 Mechanical properties of the fibres used in the roll wrapped tubes. 25

3.1 Boundary conditions of the different simulations. 32

4.1 Materials and profiles of the tubular frame chassis. 33
4.2 Relevant mechanical properties. 34
4.3 ROHACELL® 51 WF mechanical properties [43]. 50

5.1 Summary of the achieved results. 57
5.2 Concept scoring of the different solutions. 58

6.1 Impact of the tubes' layout on torsional stiffness, mass and specific stiffness. 64
6.2 Profile selection. 64

B.1 Concept scoring of the different solutions. 81
B.2 Concept scoring, regarding driver safety. 82
B.3 Cost estimation of the materials of the chassis. 83

Intentionally blank page.

List of Figures

2.1 Twin-tube chassis of the 1934 Auto Union vehicle [3]. 8
2.2 Space frame chassis of Jaguar C-Type [4]. 8
2.3 Example of a Formula Student monocoque chassis [7]. 9
2.4 Example of a Formula Student hybrid chassis [6]. 9
2.5 Chassis of the Blade car [10]. 9
2.6 Conventional vehicle axes system [12]. 10
2.7 Squatting of the chassis when accelerating [11]. 11
2.8 Lateral bending of the chassis, top view [11]. 12
2.9 Horizontal lozenging of the chassis [11]. 12
2.10 Torsional bending of the chassis [11]. 13
2.11 Simplified car model. 14
2.12 Linear to torsion spring diagram. 15
2.13 Evolution of relative vehicle stiffness in function of the chassis' torsional stiffness. 16
2.14 Components of the primary structure. 18
2.15 Ashby Chart of Young's modulus plotted against density [17]. 19
2.16 Different types of composite tubes. 25
2.17 Sandwich panel schematics. 26

3.1 Torsional stiffness model on the tubular chassis with beam elements. . . . 30
3.2 Frontal impact model on the tubular chassis with beam elements. 31
3.3 Lateral impact model on the tubular chassis with beam elements. 32

4.1 Nominal stress-strain curve of the AISI 4130 steel [38]. 34
4.2 Vertical displacement of the wheel depending on the number of nodes, for the steel space frame modelled by beam elements. 35
4.3 Rigid (left) and flexible (right) behaviour of the suspension arms. 35
4.4 Equivalent von Mises stress in torsional stiffness test, for the steel space frame modelled by beam elements. 36
4.5 Horizontal acceleration over impact time, for the steel space frame modelled by beam elements. 37
4.6 Semi-log graph of the limits of tolerance to linear acceleration [39]. 37
4.7 Frame shape after frontal impact, for the steel space frame modelled by beam elements. 38
4.8 Lateral acceleration over impact time, for the steel space frame modelled by beam elements. 38
4.9 Frame shape after lateral impact, for the steel space frame modelled by beam elements. 39

4.10 Tube coupling detail, after treatment in FEMAP. 39
4.11 Detail of the coupling between the suspension arms beam and the chassis shell. 40
4.12 Vertical displacement of the wheel centre convergence plot, for the steel space frame modelled with shell elements. 41
4.13 Equivalent von Mises stress in torsional stiffness test, for the steel space frame modelled with shell elements. 41
4.14 Horizontal acceleration over impact time, for the steel space frame modelled with shell elements. 42
4.15 Frame shape after frontal impact, for the steel space frame modelled with shell elements. 43
4.16 Lateral acceleration over impact time, for the steel space frame modelled with shell elements. 43
4.17 Frame shape after lateral impact, for the steel space frame modelled with shell elements. 44
4.18 Composite space frame geometry. 44
4.19 Equivalent von Mises stress in torsional stiffness test, for the composite space frame. 46
4.20 Hashin's criteria (maximum value of all layers). 46
4.21 Horizontal acceleration over impact time, for the composite space frame. . 47
4.22 Frame shape after frontal impact, for the composite space frame. 47
4.23 Lateral acceleration over impact time, for the composite space frame. . . . 48
4.24 Frame shape after lateral impact, for the composite space frame. 48
4.25 Monocoque chassis geometry. 49
4.26 ROHACELL® 51 WF stress-strain compression curve [43]. 50
4.27 Cutaway view of the monocoque meshed geometry. 51
4.28 Distorted element in the frontal impact case. 51
4.29 Deformation detail on the suspension arms attachments points. 52
4.30 Stresses in torsional stiffness test. 53
4.31 Hashin's criteria (maximum value of all layers). 53
4.32 Horizontal acceleration over impact time, for the monocoque chassis. . . . 54
4.33 Shape of the structure at $3.26 \cdot 10^{-3}$ seconds. 54
4.34 Detail of the front section. 54
4.35 Lateral acceleration over impact time, for the monocoque chassis. 55
4.36 Energy history over impact time (ALLAE – "artificial" strain energy, ALLDC – energy dissipated by distortion control, ALLIE – total strain energy). 55
4.37 Frame shape after lateral impact. 56

6.1 Different tubes placements under analysis. 63
6.2 Tensile matrix failure, bottom view. 65
6.3 Shape of the structure after impact, without the effect of the stiffness of the engine. 66
6.4 Shape of the strucutre (maximum deformation, at $t = 3.8 \cdot 10^{-2}$ s), with a deformation scale factor of 0.5. 66

7.1 Geometry and profiles used in the new chassis. 67

7.2 Final solution of the chassis (right), compared to the previous steel space frame (left). 68
7.3 Equivalent von Mises stress in torsional stiffness test. 69
7.4 Tensile matrix failure criterion, with two opposite 4000 N loads. 69
7.5 Horizontal acceleration over impact time. 70
7.6 Shape of the structure (maximum deformation, at t = $3.2 \cdot 10^{-2}$ s). 70
7.7 Lateral acceleration over impact time. 71
7.8 Shape of the structure after impact. 71

A.1 Cockpit opening template (left) and cockpit internal cross section template (rigth) [1]. 79
A.2 95^{th} percentile male placement [1]. 79

Intentionally blank page.

List of Symbols

The following list describes several symbols that will later be used within the body of the document:

Δz	Displacement along the z axis
ν	Poisson's ratio
ϕ	Angular deflection on the x axis
ρ	Specific mass
σ_{c}	Compressive yield strength
$\sigma_{\mathrm{Hyd,c}}$	Hydrostatic compressive yield strength
σ_{u}	Ultimate strength
σ_{y}	Yield strength
τ	Moment of force at the torsion spring
a_{x}	Acceleration on the x axis
a_{y}	Acceleration on the y axis
a_{mean}	Average acceleration
CG_{height}	Centre of gravity height
E	Young's modulus
F	Force
k_{chassis}	Stiffness of the chassis
k_{l}	Linear stiffness
k_{susp}	Stiffness of the suspension system
k_{t}	Torsional stiffness
k_{veh}	Stiffness of the vehicle
L	Distance

LT_{lat}	Lateral load transfer
LT_{lon}	Longitudinal load transfer
M	Moment of force
m	Mass
t	Thickness of the section
T_{w}	Track width
W_{b}	Wheelbase

Part I

Introduction and background

Chapter 1

Introduction

1.1 Formula Student competition

"Engenius - UA Formula Student" is a team of students of the University of Aveiro, created in 2006, whose goal is to compete in the Formula Student competition. Formula Student is an educational engineering competition for university students from all around the world, in which they design, fabricate, develop and compete with formula-style racing cars. The aim is to provide students with a more real engineering experience, while developing soft skills such as time management, teamwork or business planning and project management.

"Teams are to assume that they work for an engineering firm that is designing, fabricating, testing and demonstrating a prototype vehicle", and the vehicle should be high performance. In addition to vehicle performance, there are other design factors as "aesthetics, cost, ergonomics, maintainability and manufacturability" [1].

The teams' cars are evaluated according to several parameters. In the static events, the business plan, cost and manufacturing as well as the engineering design are evaluated. In the dynamic side, the car should complete a series of events: skid pad, acceleration, autocross and endurance (with the associated efficiency being evaluated). For safety reasons, before the dynamic events the vehicle must pass a tight technical scrutineering to make sure it fully complies with the competition rules, and it must also undergo a tilt test as well as a noise and braking test.

1.2 Problem definition and objectives

The main objective of this work is to model and perform numerical simulations and structural analyses of chassis structures. The ultimate goal is to develop a new solution with major improvements over existing ones.

The competition rules define the chassis as the "structural assembly that supports all functional vehicle systems" [1]. Being a structural element, it must be able to withstand the different load scenarios that arise while driving, as well as ensure the safety of the driver.

Therefore, throughout this work several options and materials are analysed in regards to their structural and crash behaviour, in order to obtain a chassis that not only complies with the rules of the competition, but is also lightweight and torsionally stiff.

1.3 Reading guide

The present dissertation document is organised as follows:

- In Chapter 2 the foundations of sports cars' chassis are addressed. From the types of frames and loading scenarios, to the most suitable materials, dependant on the type of frame. Additionally, to make the document more easily understating, the name of the main components of the chassis is given. Furthermore, the importance of ergonomics is explained.
- Chapter 3 covers the procedures that were done in order to compare the various types of chassis under analysis. The parameters of evaluation and the setup of the finite elements analyses (FEA) is also mentioned.
- Chapter 4 describes the FEA model's definition of each type of chassis under consideration and provides an analysis of the results obtained.
- In Chapter 5 a critical review of the chassis, in respect to the parameters of evaluation that were established in Chapter 3, is made.
- The new chassis solution is covered in Chapter 6. Several aspects that should be taken into account in order to improve the chassis (in relation to the previous one) are addressed. Afterwards, the design process is described, and a brief analysis for improving the frame's stiffness is shown.
- In Chapter 7, the final version of the chassis, after the necessary modifications were made, is presented and some analyses are performed with the aim of demonstrating that the finalised chassis shows considerable improvements over the previous ones.
- Lastly, there is a brief extension on the conclusions of this work, as well as future recommendations.

Chapter 2

Theoretical foundations

2.1 Introduction

First and foremost, it is important to have a basic understanding of chassis design and vehicle dynamics. In this chapter the following topics will be extend upon: main chassis types, loads that the structure is subject to and its influence in the vehicle dynamics, and also a discussion on the suitable materials that can be considered.

2.2 Chassis types

Before the Second World War, sports cars were of the girder type, and its design owed more to bridge-building than to light engineering [2]. At that time, only the bending behaviour of the structure was taken into account, with no considerations about torsion behaviour. Although the stiffness has an important influence on the vehicle's handling and vibrational behaviour, the fact that car bodies were made of timber, leading to a low-stiffness body structure, was a positive factor since it allowed more deformation. When metal bodies started being used, the difference between the chassis stiffness and body stiffness typically led to body material damage [3].

2.2.1 Twin-tube or ladder frame chassis

When the chassis torsional stiffness became a design concern, engineers developed a new chassis layout. In 1934 Auto Union and Mercedes-Benz introduced the twin tube chassis (Figure 2.1). This layout, very usual in trucks and some off-road vehicles, includes two symmetrical lateral beams and several transverse cross members, resembling a ladder. This type of chassis has a higher torsional stiffness than the girder one, but the increase of torsional stiffness results in a heavier frame [2].

2.2.2 Space frame chassis

In 1952, Jaguar C-Type was introduced with a space frame chassis (Figure 2.2). In this layout, the chassis is a skeletal frame, with tubes triangulated in such a way that they are loaded only in compression or traction [4]. Therefore, the position of the tubes can be optimised to increase stiffness while reducing the weight. However, due to the

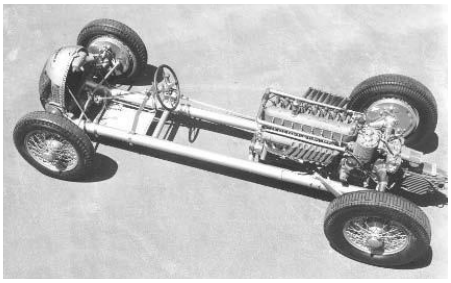

Figure 2.1: Twin-tube chassis of the 1934 Auto Union vehicle [3].

large number of tubes and some geometrically-complex nodes, manufacturing is more demanding when compared to previous frames.

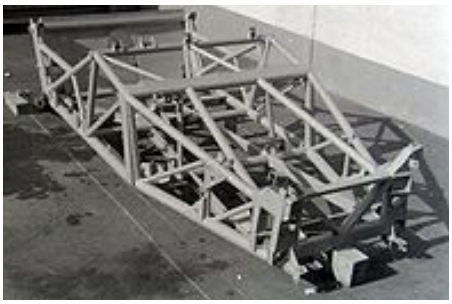

Figure 2.2: Space frame chassis of Jaguar C-Type [4].

2.2.3 Monocoque chassis

The first monocoque chassis appeared in 1962 with Formula One's Lotus 25 [5]. The monocoque is usually a one-piece component, with the chassis and the body being the same component (Figure 2.3). This type of frame has a high stiffness with low weight, being able to absorb all loads generated when driving. As new materials and manufacturing techniques were developed, the frames went from aluminium monocoques to the most advanced sandwich monocoques with carbon fibre reinforced plastics (CFRP). However, this type of frame has some disadvantages, such as the high cost and challenging design and manufacturing [6]. Furthermore, the ease of repair and modification, as well as the competition's technical inspection, are more complex.

2.2.4 Hybrid chassis

Some Formula Student teams have been using a monocoque-space frame hybrid chassis (Figure 2.4). In comparison to the monocoque solution, this frame provides better heat dissipation in the engine compartment while facilitating the access to the components, which benefits the maintainability of the powertrain. However, some complication might appear between the monocoque and the tubular frame sections [8] [6].

Figure 2.3: Example of a Formula Student monocoque chassis [7].

Figure 2.4: Example of a Formula Student hybrid chassis [6].

2.2.5 Composite space frame chassis

In 2015, a Divergent Technologies subsidiary, Divergent 3D, launched what is known as the first 3D printed supercar, the Blade. 3D printing technology is used to print aluminium and titanium alloys, allowing the production of parts with complex shapes, such as those obtained with topological optimisation, thus minimising material waste and reducing weight. The chassis is a very interesting component, as it is a space frame chassis made of 3D-printed metal nodes where carbon fibre tubes are fitted (Figure 2.5). This results on a chassis weight of about 46 kg and a total car weight of 635 kg [9].

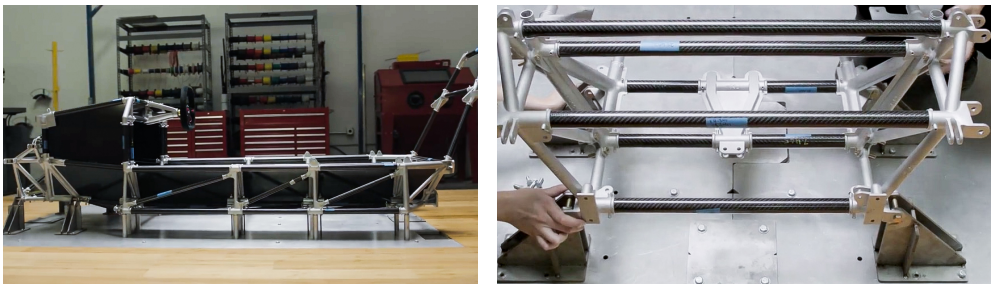

(a) Overall view. (b) Mounting detail.

Figure 2.5: Chassis of the Blade car [10].

Considering the previously described chassis types, the twin-tube will not be taken into account for several aspects. Firstly, it is the one with the lowest torsional stiffness, which is the most important structural parameter (Section 2.3.4 in the following). In order to have a reasonable value, the chassis's weight would be affected. Secondly, the location of the mounting points to fix the various components of the vehicle implies using sub-frames, thus increasing the weight as well [6].

The hybrid chassis will also not be analysed, since it is very similar to the monocoque one. Therefore, the chassis types that will be analysed in this work are the metal space frame, the composite space frame and the monocoque chassis.

2.3 Vehicle loading

Before designing a new structure, it is fundamental to understand the loads acting on it. The main deformation modes that a chassis may be subject to can be organised as follows [3] [11]:

1. Vertical bending (vertical symmetrical loads);
2. Lateral bending (lateral loads);
3. Horizontal lozenging (longitudinal asymmetric loads);
4. Longitudinal torsion (vertical asymmetric loads);
5. Crash cases.

Prior to explaining in more detail each of the load scenarios, one should know the axes convention used to describe the degrees of freedom of a vehicle (Figure 2.6). The rotation around the x, y and z axes are called roll, pitch and yaw, respectively.

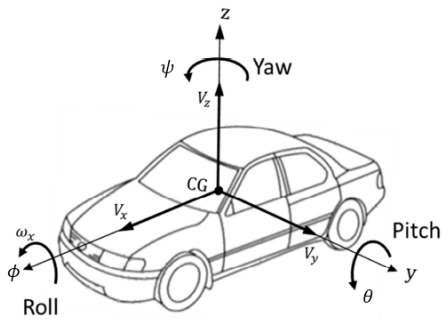

Figure 2.6: Conventional vehicle axes system [12].

2.3.1 Vertical bending case

The bending case can occur in three different situations. Firstly, it occurs when both wheels on one axle encounter a bump (vertical symmetrical loading) [3]. The other two situations are when the vehicle either accelerates or decelerates, causing longitudinal load transfers. The effect of the acceleration on the centre of gravity, which is located at

some distance from the ground, generates a moment which transfers load. When the car accelerates, the generated moment causes the chassis to squat (bending down) as Figure 2.7 indicates. Likewise, when the car brakes, the chassis will dive [6] and the rear wheels will be partially unloaded, losing braking capacity [13].

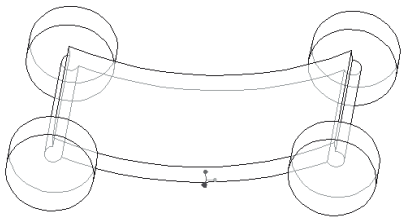

Figure 2.7: Squatting of the chassis when accelerating [11].

In Equation 2.1, it can be seen that the longitudinal load transfer can be minimised with the reduction of the vehicle's weight (m) and centre of gravity height (CG_{heigth}) or with a longer wheelbase (W_{b}) [13]. Although a longer wheelbase will reduce the effect of longitudinal load transfer (LT_{lon}), the handling while cornering will be affected. Besides that, the wheelbase belongs to suspension's scope, so the focus will be in reducing the chassis's weight and centre of gravity height.

$$LT_{\text{lon}} = \frac{m \cdot CG_{\text{height}}}{W_{\text{b}}} \cdot a_{\text{x}} \quad [\text{N}] \tag{2.1}$$

2.3.2 Lateral bending case

While on cornering, the centrifugal force, that is resisted by the tires and frame members, causes lateral bending (Figure 2.8). Furthermore, as with the longitudinal load transfer, the centrifugal force acts on the centre of mass, creating a moment of force on the roll axis, which transfers some of the load from the inside tires to the outside tires. Roll should be minimised as it causes wheel camber, affecting tire adhesion, and because "the more stable the car is, the better it responds to direction changes" [6].

Just like the longitudinal load transfer, the lateral load transfer (LT_{lat}) can be minimised with a lower mass and height of centre of gravity, and with a larger track width (T_{w}) (Equation 2.2) [13].

$$LT_{\text{lat}} = \frac{m \cdot CG_{\text{height}}}{T_{\text{w}}} \cdot a_{\text{y}} \quad [\text{N}] \tag{2.2}$$

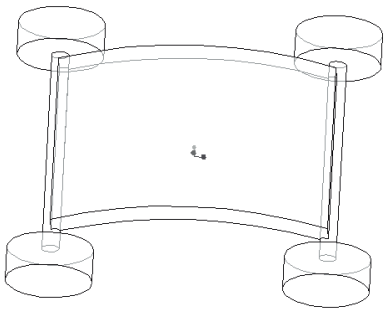

Figure 2.8: Lateral bending of the chassis, top view [11].

2.3.3 Horizontal lozenging

When opposite wheels are subjected to unequal loads, the chassis deforms into a parallelogram shape as shown in Figure 2.9. These forces may be caused by vertical variations in the pavement, or when one side of the car has better traction than the other. It can also occur under heavy braking, when one of the tires locks up [11] [6].

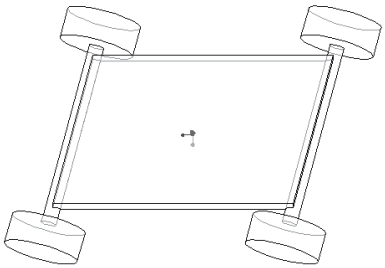

Figure 2.9: Horizontal lozenging of the chassis [11].

2.3.4 Longitudinal torsion

This case occurs whenever loads appear on one or two opposite tires of the car [11], for instance when one of the wheels hits a bump [3] or takes a corner (Figure 2.10). When the car takes a corner, ideally a lateral load transfer from the inside rear tire, for instance, would occur to the outside rear tire. However, if while entering the corner the car brakes, a portion of the load will be transferred to the outside front tire, and the overload of it can result in understeer. Furthermore, when the car accelerates while exiting the corner, the load transfer to the back will unload the front tires which could also result in understeer [13]. In order to obtain a good handling balance, the load transfer distribution must be optimised with many small suspension adjustments, which can only be done if the chassis is stiff enough [14].

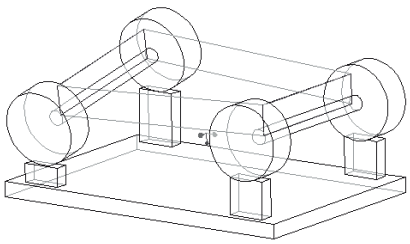

Figure 2.10: Torsional bending of the chassis [11].

2.3.5 Crash cases

In case of impact, it is crucial that the structure deforms in such a way that it absorbs the impact energy and provides safe deceleration levels, while protecting the driver's body. In Formula Student dynamic events, the cars compete against the clock (time trial), so the chance of a crash between two vehicles is low.

In this project, two types of collision were considered: frontal and lateral impact. The competition rules state that the vehicle must have a frontal impact attenuator that should meet some requirements at an impact speed of 7 m/s (25.2 km/h). Within this dissertation work, it was decided to go a little further, and as Formula Student cars may exceed 100 km/h, European New Car Assessment Programme (NCAP) tests were taken into account. For the frontal impact scenario, the car impacts with a rigid barrier at a speed of 50 km/h, and for the side impact the car impacts with a rigid circular barrier, at a speed of 32 km/h.

2.4 Torsional stiffness

The torsional stiffness gives the relationship between the applied torque along the longitudinal axis (x axis) and the resulting amount of twist. As stated in [15], the main goal when designing a chassis should be the improvement of the torsional stiffness, since "a chassis that has good torsional stiffness also has adequate bending stiffness. If care is taken to insure adequate torsional stiffness, bending is not likely to cause a problem". Reference [11] also states that torsional stiffness "is generally thought to be the primary determinant of frame performance for a FSAE racecar".

2.4.1 Torsional stiffness determination

In order to obtain the value of the torsional stiffness, opposing vertical loads are applied to both front wheel centres, while the rear ones are constrained. As stated in [8], "this appears to give the most realistic results considering the analogy with the real torsional load". Afterwards, the torsional stiffness is computed with the following equation:

$$k_t = \frac{M}{\phi} \quad [\text{Nm/rad}]\,. \tag{2.3}$$

The torsional moment, M, is obtained with the applied loads (F) and the distance (L) from its point of application (wheel centre) to the x axis

$$M = 2FL \quad [\text{Nm}]\,, \tag{2.4}$$

and the angular deflection, ϕ, is given by

$$\phi = \arctan\left(\frac{\Delta z}{L}\right) \quad \left[\text{rad}^{-1}\right], \tag{2.5}$$

where Δz is the vertical displacement.

2.4.2 Torsional stiffness target

The stiffer the chassis is, the easier it is to control the lateral load transfer distribution of the car, thus improving its handling. Furthermore, a stiffer chassis is less prone to fatigue, which could result in failure [15]. The downside of increasing stiffness is the inherent weight increase, therefore the torsional stiffness must take into account the chassis's weight – specific stiffness.

It is convenient to look at the evolution of the overall stiffness in function of the chassis stiffness. In order to do that, a simplified model of the car, as shown in Figure 2.11, is used. Each wheel's spring is represented, and the chassis is characterised as one torsion spring. Total vehicle resistance to torsional stiffness, k_{veh}, can be obtained assuming the principal of superposition [11]:

$$\frac{1}{k_{\text{veh}}} = \frac{1}{k_1} + \frac{1}{k_2} + \frac{1}{k_3} + \frac{1}{k_4} + \frac{1}{k_{\text{chassis}}} \tag{2.6}$$

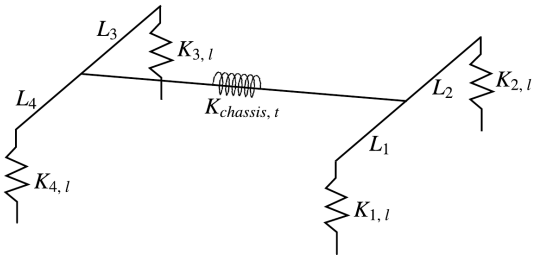

Figure 2.11: Simplified car model.

To combine linear and torsion springs, it is desirable to find a way to represent the linear springs as torsion ones (Figure 2.12). A force applied to the linear spring produces a moment of force at the torsion spring on the other end

$$\tau = FL\cos(\theta) \quad [\text{Nm}]. \tag{2.7}$$

Moreover, the Hooke's Law for the torsion spring

$$\tau = -k_{\text{t}} \cdot \theta \quad [\text{Nm}] \tag{2.8}$$

can be rearranged with Equation 2.7. If the direction is ignored, we obtain the following expression:

$$k_t = \frac{FL\cos(\theta)}{\arctan\left(\frac{d}{L\cos(\theta)}\right)} \quad [\text{Nm/rad}]. \tag{2.9}$$

For relatively small values of θ, we have:

$$\cos(\theta) \approx 1. \tag{2.10}$$

With the previous simplification, and as $L \gg d$, the value inside the arctan() of Equation 2.9 will be very small, so the following simplification can be used:

$$\tan(\alpha) \approx \alpha \Rightarrow \arctan\left(\frac{d}{L}\right) \approx \frac{d}{L}. \tag{2.11}$$

By combining Equation 2.9 with 2.10 and 2.11 we obtain

$$k_{\text{t}} \approx \frac{FL^2}{d} \quad [\text{Nm/rad}]. \tag{2.12}$$

If we compare the Hooke's Law for linear springs

$$F = -k_{\text{l}} \cdot x \quad [\text{N}] \tag{2.13}$$

with the Equation 2.12, the following relation is found:

$$k_{\text{t}} \approx k_{\text{l}} \cdot L^2 \quad [\text{Nm/rad}]. \tag{2.14}$$

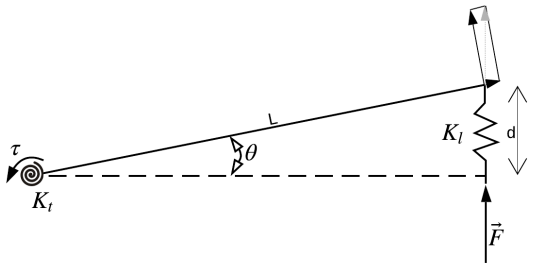

Figure 2.12: Linear to torsion spring diagram.

Finally, the vehicle resistance to torsional stiffness can be determined with the following expression:

$$\frac{1}{k_{\text{veh}}} = \frac{1}{K_{1,\text{l}} \cdot L_1^2} + \frac{1}{K_{2,\text{l}} \cdot L_2^2} + \frac{1}{K_{3,\text{l}} \cdot L_3^2} + \frac{1}{K_{4,\text{l}} \cdot L_4^2} + \frac{1}{k_{\text{chassis, t}}} \tag{2.15}$$

Using MATLAB, with a front track width of 1150 mm and a rear one of 1250 mm, and a front and rear spring stiffness of 150 N/mm and 200 N/mm, respectively, the relative vehicle stiffness is plotted in function of the chassis torsional stiffness (Figure 2.13). The relative vehicle stiffness is used in order to facilitate comparison with the rigid case, and is obtained by dividing the vehicle stiffness by the suspension stiffness:

$$k_{\text{rel}} = \frac{k_{\text{veh}}}{k_{\text{susp}}}, \tag{2.16}$$

where

$$k_{\text{susp}} = \frac{1}{K_{1,1} \cdot L_1^2} + \frac{1}{K_{2,1} \cdot L_2^2} + \frac{1}{K_{3,1} \cdot L_3^2} + \frac{1}{K_{4,1} \cdot L_4^2}. \tag{2.17}$$

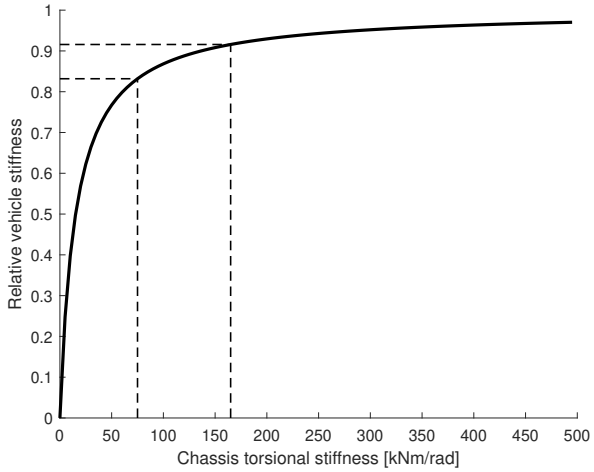

Figure 2.13: Evolution of relative vehicle stiffness in function of the chassis' torsional stiffness.

It can be observed that the curve is logarithmic, so increasing the chassis stiffness from a certain point brings little benefit in terms of vehicle stiffness. At a certain point, seeing an increase in vehicle stiffness implies having a large increase in chassis stiffness, which affects the chassis weight.

A good target is between 75 and 165 kNm/rad, which is in line with [8], which states that the chassis torsional stiffness of Formula Student vehicles is between 50 and 300 kNm/rad, with the competition average in the 120 kNm/rad. Regarding the specific stiffness, values are in the 1.7-15 kNm/(rad · kg) range, with the average vehicles in the 4.8 kNm/(rad · kg).

2.5 Loads in the wheels

The team's suspension department has done some studies on the loads that arise in several scenarios: cornering with an lateral acceleration of 2.2 g, braking with a deceleration of 2.2 g and passing through a 100 mm deep hole. The loads acting in the inside front wheel (the critical case) are shown in Table 2.1. The maximum vertical load of 3530 N will be of importance to simulate the torsional stiffness of the chassis.

Table 2.1: Loads on the front wheel, for different driving scenarios.

Loads	Cornering	Braking	Hole	Total
F_x [N]	0	-3430	-1600	-5030
F_y [N]	3775	0	0	3775
F_z [N]	1340	1130	1060	3530
M_x [Nm]	700[1]	0	0	700
M_y [Nm]	0	540	0	540
M_z [Nm]	0	0	0	0

2.6 Chassis components

Throughout the work some specific names of chassis components are mentioned. Basically, a Formula Student chassis consists of 3 sections: the front section is where the front suspension is attached, and where the driver's legs are; the middle zone is where the pilot's seat is located; and finally the rear section is where the powertrain and drivertrain are usually located, and also where the rear suspension is attached.

In Figure 2.14 the main chassis components are labelled. The front bulkhead defines the forward plane of the chassis. It is where the impact attenuator is fixed, and provides protection for the driver's feet. The main and front hoops provide protection in case of a rollover, and the tubes alongside the driver (between the hoops and from the chassis floor to a height between 240 and 320 mm) define the side impact structure [1].

2.7 Ergonomics

Although the chassis should be as compact as possible, in order to minimise weight, the driver must have easy access to all controls, while being in a comfortable and safe position. The driver should be able to turn the wheel comfortably and safely (without any part of the body being outside of the cockpit), and they must be able to exit the vehicle in less than 5 seconds [1]. Also, to ensure the driver's safety, the head restraint and the harness attachment points should be well positioned and in accordance with the rules.

[1]This value is from [8], as the suspension department was not able to provide it. Since the loads depend on the vehicle characteristics such as weight, track width and wheel base, there may be some differences.

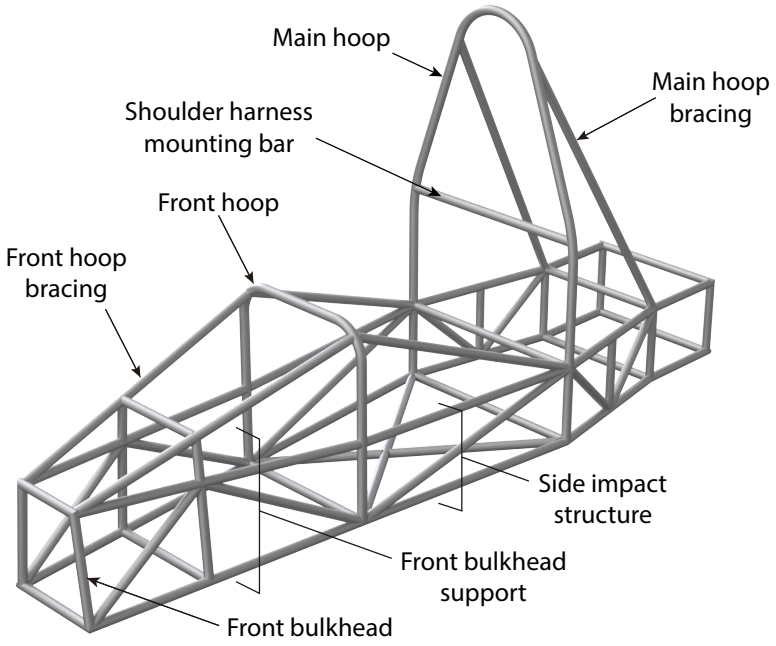

Figure 2.14: Components of the primary structure.

Regarding the cockpit main dimensions, the most important factor to take into account is the cockpit opening and internal section, and also the positioning of the 95^{th} percentile male placement. To assess the size of the cockpit opening, the template shown on the left of Figure A.1 (Appendix A) must pass vertically from the cockpit opening to bellow the upper side impact member. Regarding the cockpit internal section, the template shown on the right should pass from the cockpit opening to a point 100 mm rearwards of the pedals [1].

Formula Student rules state that the vehicles should be able to accommodate drivers up to the size of a 95^{th} percentile male. In Figure A.2 the placement of a 95^{th} percentile male template is shown, giving the minimum dimensions that must be fulfilled. Regarding the rollover, and as per the rules, the helmet of the percentile should be 50 mm bellow from the straight line connecting the top of the hoops.

2.8 Materials

2.8.1 Material selection

A good starting point before designing a chassis is selecting the most suitable material, by defining the requirements it must meet. As seen in Section 2.3, the most important aspect of a chassis is its stiffness (mainly torsional), while obviously ensuring its strength.

Ideally, on a space frame chassis, tubes are mainly loaded in tension or compression. However, some tubes will experience bending, as it is difficult to have all the chassis members perfectly triangulated. Also, bending can occur in a side impact scenario, for instance. Having this in mind, we should aim to have a material with good stiffness in those three cases. To maximise the stiffness while minimising the tube mass, the following performance indexes should be maximised [16]:

- Tension: $\frac{E}{\rho}$;
- Compression and bending: $\frac{E^{\frac{1}{2}}}{\rho}$,

where E is the Young's modulus, and ρ is the specific mass.

The same applies for a monocoque frame, so tensile, compressive and bending scenarios can occur. The performance indexes that are used in order to maximise the stiffness of a flat plate while minimising the mass, are [16]:

- Tension: $\frac{E}{\rho}$;
- Compression and bending: $\frac{E^{\frac{1}{3}}}{\rho}$.

With an Ashby Chart (Figure 2.15) performance indexes of several potential materials can be easily obtained – Table 2.2. Considering that all the indexes have the same weighting factor, and scaling the values in relation to the highest one, the results for both the space frame and the monocoque chassis are listed in the last two columns. For a tubular chassis, the following order is obtained:

$$\text{CFRP} > \text{Bamboo} > \text{Al alloy} > \text{GFRP}\ ^{2} > \text{Steel alloy},$$

and, for a monocoque:

$$\text{CFRP} > \text{Bamboo} > \text{Al alloy} > \text{GFRP} > \text{Steel alloy}.$$

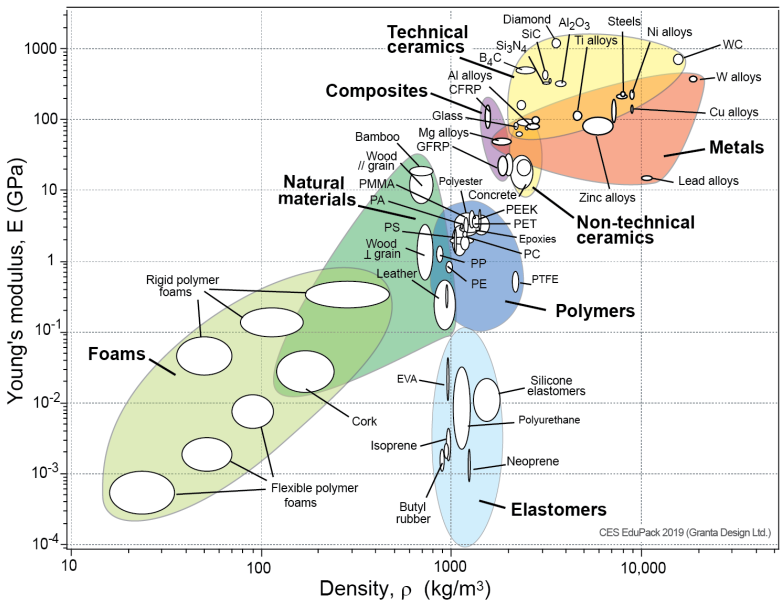

Figure 2.15: Ashby Chart of Young's modulus plotted against density [17].

For both solutions, the CFRP is the best material, from a stiffness standpoint. The second best material seems to be bamboo, but if the same analysis is done for maximising

[2] Glass fibre reinforced plastics.

the strength while minimising the mass (using the performance indexes stated in [16]), the following sequence is obtained for a space frame chassis:

CFRP (100.0 %) > GFRP (19.0 %) > Steel alloy (11.8 %) > Al alloy (9.5 %) > Bamboo (9.2 %),

and, for a monocoque:

CFRP (100.0 %) > GFRP (29.3 %) > Bamboo (24.5 %) > Al alloy (16.3 %) > Steel alloy (13.9 %).

For the two architectures, both in strength and stiffness, the best option is, by far, the CFRP. Regarding the metals, general-purpose aluminium alloys seems to be a better solution than general-purpose steel alloys. Although it has a 2% lower strength performance index in the space frame chassis, its effect is outweighed by the 13% difference in the stiffness index. However, aluminium is more expensive, and the welding process is more complex.

In relation to bamboo, it seems to be an interesting material for a tubular chassis, and also a good option for a monocoque one. However, bamboo composite tubes (for the space frame) or fibres textiles (for the monocoque) are not easy to find on the market.

When choosing between metallic and composite materials, the way in which the energy from impacts is absorbed must be taken into account. Most widely used metals are ductile, having a considerable plastic zone, which allows them to absorb energy while deforming. Whereas composite materials are brittle, so most of the energy is dissipated in the failure process, which can have an impact on the safety of the structure, especially if it suffers loads that were not expected during the design process.

Table 2.2: Performance indexes of potential materials.

Material	E [MPa]	ρ $[\frac{\text{kg}}{\text{m}^3}]$	$\frac{E}{\rho}$ $[\frac{\text{MPa}\cdot\text{m}^3}{\text{kg}}]$	$\frac{E^{\frac{1}{2}}}{\rho}$ $[\frac{\text{MPa}^{\frac{1}{2}}\cdot\text{m}^3}{\text{kg}}]$	$\frac{E^{\frac{1}{3}}}{\rho}$ $[\frac{\text{MPa}^{\frac{1}{2}}\cdot\text{m}^3}{\text{kg}}]$	$\text{PI}_{\text{S.F.}}$ [3] [%]	$\text{PI}_{\text{Mon.}}$ [4] [%]
Al alloys	70	2700	0.0259	0.0031	0.0015	44.6	41.2
Steel alloys	205	7800	0.0263	0.0018	0.0008	31.0	27.6
CFRP	105	1700	0.0618	0.0060	0.0028	91.2	82.7
GFRP	25	1900	0.0132	0.0026	0.0015	35.3	34.5
Bamboo	18	700	0.0257	0.0061	0.0037	80.5	80.5

2.8.2 Composite materials

Within this section, reference [18] was the main source of information. Composites main components are the fibres, that provide most of the stiffness and strength, and the matrix that binds the fibres together and provides stress transfer among fibres and protects them from chemical attack and abrasion. A thin plate or shell of fibre-composite material is known as lamina or ply.

[3] Performance index of the space frame chassis.
[4] Performance index of the monocoque chassis.

2.8.2.1 Fibres

Fibres are lightweight, stiff and strong elements. Their strength comes from the orientation of the molecules along the fibre, and also from the reduced number of defects. There is a wide variety of fibres, and they can be classified according to their length (short, long or continuous), stiffness (low, medium, high or ultra high modulus) and chemical composition (organic or inorganic).

Continuous fibres are used when maximum achievable stiffness and strength are desired, as the load is carried mostly by the fibres orientated along the direction of the load. Using discontinuous fibres is less costly, but only 50% of the strength and 90% of the stiffness of a continuous fibre composite material can be reached. Furthermore, since the load is transferred from fibre to fibre through the matrix, the quality of the fibre-matrix interface is of great importance.

Fibre textiles can be unidirectional, or they can be a fabric with different types of orientations. Unidirectional fibres are suited for when reinforcement is desired in only one direction. In unidirectional fabrics there are some thin cross-orientated fibres, usually from a lower grade material, to hold everything in place.

Regarding the 2D fabrics, these can be nonwoven or woven fabrics. A nonwoven fabric, known as a mat, is made of randomly orientated fibres, leading to isotropic properties in the composite. Despite their low cost, the mechanical properties of this kind of reinforcement are low. On the other hand, the woven fabrics are made of interlaced fibres in weaving machines, therefore different weaving patterns can be produced in order to have the most desirable properties.

2.8.2.1.1 Glass fibres

Glass fibres are flexible, lightweight and inexpensive, being the most commonly in low-cost applications. The most used types are E-glass and S-glass. E-glass is the preferred structural reinforcement due to the high tensile strength (about 1.75 GPa), good chemical resistance and low cost. On the other hand, S-glass has the highest strength (about 2.10 GPa) and a better stability in humid environments. However, they cost three to four times more than E-glass, so when stronger fibres are needed, low cost carbon fibres are used instead.

2.8.2.1.2 Carbon fibres

Carbon fibres are lightweight, strong fibres with excellent chemical resistance. Their properties are strongly dependant on the raw material and the manufacturing process. The stiffness of carbon fibres is controlled by their thermal treatment, so carbon fibres are available in a broad range of stiffness values, unlike glass fibres. As they are also stiffer than glass fibres, they provide better fatigue characteristics (due to less strain in the matrix), so lower safety factors are used. However, due to the high rigidity, carbon fibres have low shock resistance. Another limitation is the high cost, that can be justified when weight savings offer a large payoff.

2.8.2.1.3 Basalt fibres

Basalt fibres are a fairly new type of fibres, made of the volcanic rock basalt. They have high strength and stiffness, good chemical and thermal stability and good corrosion

resistance. Despite having better mechanical properties than glass fibres, they cost less than the carbon ones.

2.8.2.1.4 Synthetic organic fibres

The organic fibres used in composites are polymeric fibres and due to their very low density, high values of specific strength and stiffness values can be achieved. Aramid fibres (aromatic polyamide) are polymer fibres that are often used in impact and ballistic protection, due to their high energy absorption during failure. However, they have low compressive strength, besides creeping, absorbing humidity and being sensitive to ultraviolet light. They also have a tensile strength reduction of about 75% at 177 °C.

2.8.2.2 Matrix

Besides holding the fibres together and transferring loads, the matrix carries transverse and intralaminar stresses. Furthermore, the properties of the matrix determine the working conditions for the composite, such as temperature range and chemical and abrasion resistance.

Matrix materials are usually thermoset polymers, because of their ease in processing and wide range of performance. A thermoset matrix is formed by the chemical transformation of a resin system. As this type of resins has low viscosity, excellent impregnation of the fibre reinforcement and high processing speeds are achieved.

The most common thermoset resins are: polyesters, vinyl ester, epoxy and phenolic. Phenolic resins are normally used in fire related aplications and are more difficult to process, so they are not discussed here.

2.8.2.2.1 Polyester resins

This type of resins are very versatile, so they can be used in various applications and with different processes. They have moderate physical properties, but they are not costly, so a high performance/cost ratio is achieved.

2.8.2.2.2 Vinyl ester resins

Vinyl ester resin have higher elongation to failure than polyester resins, allowing more load to be transferred to the reinforcement. They also have better corrosion resistance. Their properties and cost are between the ones of the polyester and the high-performance epoxy resins.

2.8.2.2.3 Epoxy resins

Epoxy resins are considered high performance resins, as they have a higher elongation to failure and higher service temperature than other resins. Besides that, they shrink less, giving them excellent bond characteristics when used as adhesives (epoxies are used as adhesives for aircraft honeycomb structures, for instance). Their cure process is simpler, as it can be achieved in a range of temperatures from 5°C to 150°C.

2.8.3 Space frame chassis

2.8.3.1 Metal tube

For steel tubes, Formula Student rules state the mechanical properties that must be used for the calculations required for certain documents inherent to the competition [1]:

$$E = 200 \text{ GPa};$$
$$\sigma_{\text{y}} = 305 \text{ MPa};$$
$$\sigma_{\text{u}} = 365 \text{ MPa};$$

where σ_{y} is the yield strength and σ_{u} is the ultimate strength.

Many teams, including "Engenius - UA Formula Student", have chosen to use AISI 4130 steel, a metal with a high strength-to-weight ratio. The steel provided to the team has a yield strength of 805 MPa and an ultimate strength of 876 MPa, according to the supplier. One might think that with these mechanical properties the weight of the chassis can be reduced using less material. However, for safety reasons, there are minimum material requirements for the members of the primary structure, as it can be seen in Table 2.3.

Table 2.3: Minimum material requirements for steel tubes [1].

Item or application	Wall thickness [mm]	Cross sectional area [mm^2]	Area moment of inertia [mm^4]
Main and front hoops, shoulder harness mounting bar	2.0	175	11320
Side impact structure, front bulkhead, roll hoop bracing, driver's restraint harness attachment (except as noted above)	1.2	119	8509
Front bulkhead support, main hoop bracing supports	1.2	91	6695

Moreover, as 4130 steel has a percentage of Cr ranging from 0.80 up to 1.10, it is considered as an alloyed steel. Thus, according to the rules, the team must include tests and documentation in the Structural Equivalent Spreadsheet to show structural equivalency to the minimum material properties for steel [1]. Another complexity of using this steel is the need to normalise the structure after welding operations, because of the possibility of catastrophic failures in the heat-affected zone (HAZ) [19]. For small wall thickness, using ER70S-2 or ER70S-6 TIG rods, which have a lower strength than 4130, post-weld heat treatment can be avoided [20].

A good option to 4130 steel is the cheaper cold drawn seamless tube (CDS) [19]. CDS is a low-carbon steel, and has a substantial high strength to weight ratio as well as tight tolerances, good machinability and a good surface finish [21]. The most common used steel series for CDS are the AISI 1018 and the 1026 steel. With the 1026 steel, an yield strength of 520 MPa and an ultimate strength of 585 MPa are achieved, which are

superior to the mechanical properties stated in the rules [22]. Regarding the chemical composition, all elements are within the range defined in the rules (maximum content of 0.3% C, 1.7% Mn and 0.6% of any other element), so no additional testing and documentation are required.

2.8.3.2 Carbon fibre composite tube

In this project, the implementation of a solution of a chassis with carbon tubes will be studied. Composite tubes, as any composite, consist of a set of fibres orientated in a certain way and bonded together by a resin. There are mainly three methods for producing composites tubes, which produce specific mechanical properties: filament winding, pultrusion and roll wrapping.

2.8.3.2.1 Filament winding

The filament winding process (Figure 2.16(a)), consists on winding composite tows under tension over a rotating mandrel. As the carriage travels up and down the length of the tube, a spiral pattern is created. Carriage movement can be programmed in order to produce different layers with different material orientations, so the mechanical properties of the tube can be tuned to the desired ones [23]. This process is very common in pressure vessels, but can be used in a range of applications such as yacht masts, bicycle rims and forks or wind turbine components [24].

2.8.3.2.2 Pultrusion

In the pultrusion process (Figure 2.16(b)), carbon filaments are pulled trough a heated die while being impregnated with epoxy resin. A mandrel is used to ensure the material holds its shape during the curing process. As the fibres are all orientated along the longitudinal axis, the tube has very good mechanical properties in tension, but poor performance in compression or torsion [25].

2.8.3.2.3 Roll wrapping

Roll wrapped tubes (Figure 2.16(c)), are made by laying up, in several orientations, multiple layers of unidirectional pre-impregnated fabrics around a mandrel. The mandrel and prepreg are then spiral wraped with heat-shrink tape, and afterwards the tube goes into an oven for curing. The heat causes the tape to shrink, compressing the layers of fabric, which maximises density and fibre to resin ratio. As the fabrics are orientated at 0° and 90°, the tube has not only good strength in the longitudinal axis, but also good bending and crush strength. That is important for real-world application, as the forces on a tube are rarely exclusively in straight compression or tension [25].

In this dissertation work, Easycomposites' roll-wrapped tubes ([27]) will be considered, for they have tubes with the appropriate dimensions commercially available, and because their mechanical properties are suitable for the intended use. According to the data provided by them, their tubes are made of five layers arranged in a 0°, 90°, 0°, 90° and 0° layup, where the 0° layers are 300 gsm (grams per square meter, g/m^2) Toray T700, and the 90° layers are 300 gsm E-Glass (80/20).

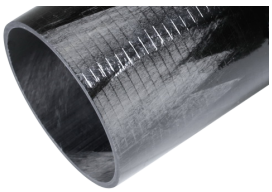

(a) Filament-wound tube [26].

(b) Pultruded tube [27].

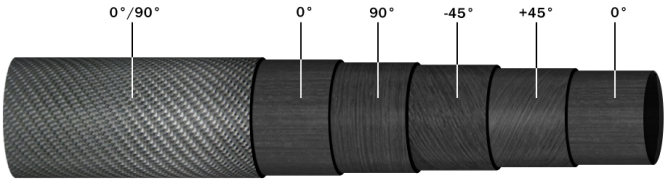

(c) Roll-wrapped tube layup example [26].

Figure 2.16: Different types of composite tubes.

Composite fibres can be considered as a transversely isotropic material, so any plane containing the fibre direction is a plane of symmetry. This type of material is described with five constants [28]. In Table 2.4, mechanical properties of E-Glass and Toray T700 are listed. It should be noted that for the sake of simplicity, E-Glass fibre is considered as being unidirectional, as 80% of the fibres are in the same direction. This simplification can be made since some weavers of 0°/90° fabrics consider a fabric with 75% of the fibres in one direction as unidirectional [29].

Table 2.4: Mechanical properties of the fibres used in the roll wrapped tubes.

Property	Toray T700 [30]	E-glass [31]
Density (ρ) [kg/m^3]	1570	1780
Young modulus 0° (E_1) [GPa]	132	40
Young modulus 90° (E_2) [GPa]	10.3	10
In-plane shear modulus (G_{12}, G_{13}) [GPa]	6.5	3.15
Out of plane shear modulus (G_{23}) [GPa]	3.91	4.32
Major Poisson's ratio (ν_{12})	0.25	0.3
Tensile strength 0° (X_t) [MPa]	2100	1432
Compressive strength 0° (X_c) [MPa]	1050	988
Tensile strength 90° (Y_t) [MPa]	24	44
Compressive strength 90° (Y_c) [MPa]	132	285
In-plane shear strength (S_{12}, S_{13}) [MPa]	75	60.6
Out-of-plane shear strength (S_{23}) [MPa]	65	22

2.8.4 Monocoque chassis

Monocoque chassis are made out of sandwich panels. Sandwich panels have a core material that is adhesively bound to two outer sheets (Figure 2.17). The external face should be made of stiff and strong materials, in order to support in-plane tensile and compressive stresses. Usually materials such as aluminium alloys, fibre-reinforced polymers or plywood are used.

The core material increases the separation of the faces, increasing the moment of inertia of the section and its sections modulus, and should be thick enough to provide high shear stiffness. Lightweight materials, normally with low modulus of elasticity, are used, such as polymeric foams, balsa wood and honeycombs, a structure of hexagonal cells normally of aluminium or an aramid polymer [32].

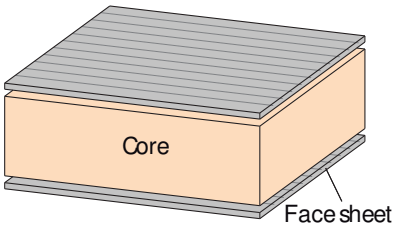

Figure 2.17: Sandwich panel schematics.

Part II

Comparison and analysis of different types of chassis

Chapter 3

Introduction and general procedures

Prior to developing a new solution for the chassis, it is necessary to know which of the previously described alternatives will be the most favourable one. In order to do that, a set of parameters will be taken into account. To do a more coherent analysis, some project variables must be fixed, so that the comparison between the different solutions can be meaningful.

The reference chassis is the steel tubular frame, the solution currently being under construction at University of Aveiro, therefore, all the other frames being analysed will have the same geometric boundaries and suspension pickup points. Obviously, this means that in each chassis several improvements could be made, including to the reference one, but it is a good starting point from which to analyse the general advantages and disadvantages of each solution.

3.1 Parameters of evaluation

In order to know which of the previously described chassis will be the most favourable one, a concept scoring will be done. The parameters which will be taken into account in the analysis, by order of importance, are:

1. Weight (30%);
2. Torsional stiffness (30%);
3. Driver safety (20%);
4. Ease of manufacture (15%);
5. Cost (5%).

The most important parameters are those related to the performance of the vehicle, with the safety of the driver having also a big impact on the choice of the most favourable chassis. Considering that the manufacture should be performed by students as much as possible, the ease of manufacture comes next. The last parameter to be considered is

the cost of the part, since the cost to the team can be reduced with the establishment of partnerships with companies.

An estimate of the weight value is obtained through SolidWorks, while the ease of manufacture is quantified taking into account the number of expected labour hours and the required expertise and facilities. The cost is calculated considering the expected material expenses. As for the torsional stiffness and driver safety, these parameters will be obtained with finite element analysis, which are explained in the next sections.

3.2 Finite element analysis tests

3.2.1 Torsional stiffness simulation

As exposed in Section 2.4.1, to obtain the torsional stiffness, opposing vertical loads are applied to both front wheel centres, while the rear ones are constrained (Figure 3.1). In this case, a safety factor is applied to the maximum vertical load listed in Table 2.1, so two loads of 5000 N are used.

Afterwards, with the applied torsional moment and the resulting angular deflection, torsional stiffness is computed with Equation 2.3. One could think that applying the loads on the suspension attachment points on the chassis would produce the same effect, as the chassis will elastically deform. However, by doing this the deflection of the suspension arms will not be taken into account, producing results that are not entirely realistic.

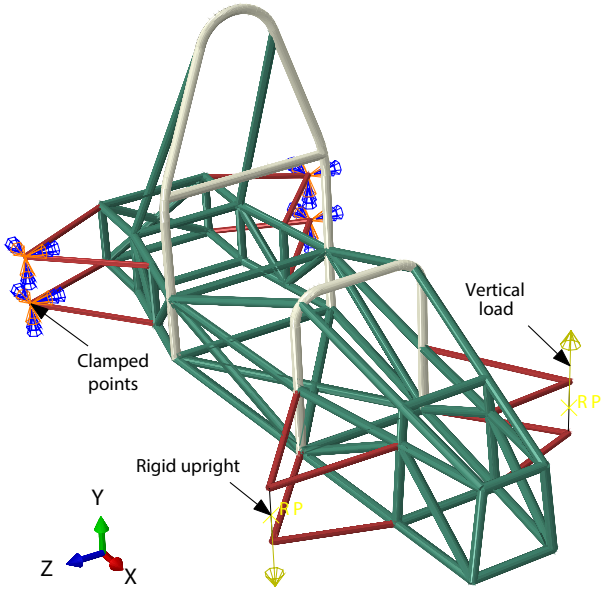

Figure 3.1: Torsional stiffness model on the tubular chassis with beam elements.

3.2.2 Driver safety

Driver safety can be evaluated, for instance, by analysing how the chassis deforms, if this deformation has an impact on the driver, and also if there is structural failure. In the

present work, two situations are considered: frontal impact and lateral impact. In both scenarios, a chassis section is fixed and a rigid mobile barrier with an initial velocity and a mass of 300 kg impacts against the structure. This mass is defined by the competition rules concerning the test conditions for the impact attenuator, and represents the typical heaviest cars found in competitions.

3.2.2.1 Frontal impact simulation

In the case represented in Figure 3.2, the rear section of the chassis is constrained to allow the full structure to absorb the impact, and the planar rigid barrier moves along the x axis with an initial velocity of 50 km/h (13,89 m/s). This velocity was selected having as reference the "front full width frontal impact" test of the European New Car Assessment Programme (Euro NCAP) [33].

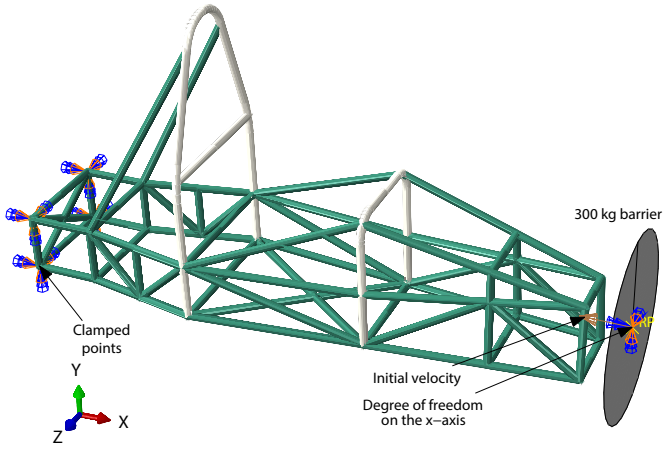

Figure 3.2: Frontal impact model on the tubular chassis with beam elements.

3.2.2.2 Lateral impact simulation

In the lateral impact simulation, represented in Figure 3.3, a circular barrier, with an initial velocity along the z axis of 32 km/h (8,89 m/s) impacts on the side impact zone of the structure. The diameter of the barrier (254 mm), and the velocity were selected having has reference the Euro NCAP's "oblique pole side impact" test [34].

In Euro NCAP's test, the pole is fixed and the car is placed on a platform that moves against it, so when the collision occurs the car moves some distance along the platform, dissipating some energy. For the sake of simplicity, in this case the chassis is fixed and the barrier is what is moving. Therefore, in addition to the rear area, the most forward section of the chassis is fixed (and not the front suspension points), so there is a larger section available to absorb the energy coming from the impact.

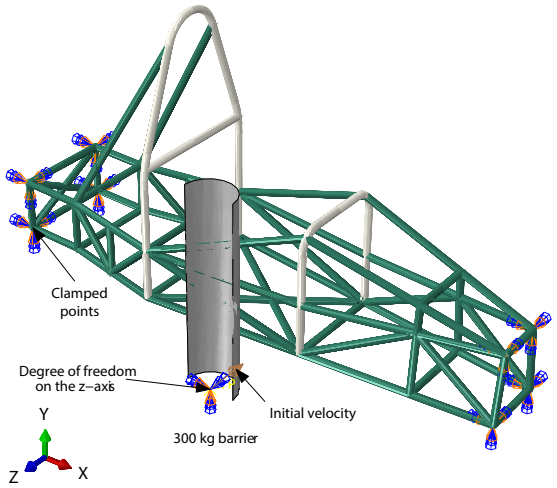

Figure 3.3: Lateral impact model on the tubular chassis with beam elements.

3.3 Simulations setup

In the previous sections, different boundary conditions were stated. Table 3.1 shows a summary of the boundary conditions used in the various simulations.

Table 3.1: Boundary conditions of the different simulations.

Test type	Boundary condition	Position
Torsional stiffness	Encastre	Chassis' rear nodes
	2000 N (opposite)	Front wheel centers
Frontal impact	Encastre	Chassis' rear nodes
	Vx_0= -13.89 m/s	Rigid barrier
Lateral impact	Encastre	Chassis' rear and front nodes
	Vz_0= -8.89 m/s	Rigid barrier

For the impact simulations, Abaqus explicit dynamics was used, and it was necessary to define the interaction between the impact barrier and the structure. On Abaqus, a normal behaviour is defined, with "hard" contact and allowing separation after contact. Tangential behaviour is also created, with a friction penalty, using a friction coefficient of 0.42 [35]. This coefficient is the kinetic friction coefficient of a steel-steel interface, considering that the impact occurs with a metallic surface, such as a rail. For the monocoque frame, made out of carbon fibre, a carbon-steel friction coefficient should be used, but no valid value was found. Nevertheless, as the frame's impacted zone will have small displacements along the impacted plane when compared with the displacement in the normal direction, using the same friction coefficient of a steel-steel interface will have a negligible impact.

Chapter 4

Finite element analysis

4.1 Steel space frame with beam elements

To have an initial idea of the structure's behaviour in different situations, a finite element model with beam elements was implemented. Simulations with beam elements are easy to implement and a fast way of assessing the general behaviour of the structure, but some details such as the tubes coupling or their crushing effect, is lost.

4.1.1 Model definition

In Figure 3.1, each of the colours represents a profile of the current vehicle's frame. Table 4.1 shows the different profiles and materials used in the simulations.

Table 4.1: Materials and profiles of the tubular frame chassis.

Region	Colour	Material	Profile
Hoops	White	AISI 4130 steel	$\varnothing_{\text{ext}} = 30$ mm, $t = 2.0$ mm
Suspension arms	Red	E190 steel	$\varnothing_{\text{ext}} = 18$ mm, $t = 2.0$ mm
Remaining	Green	AISI 4130 steel	$\varnothing_{\text{ext}} = 28$ mm, $t = 1.5$ mm

Regarding material properties, Table 4.2 lists the relevant mechanical properties of the steel alloys used in the work. For the impact cases, it is expected that the structure will plastically deform, so the stress-strain data from an uniaxial tensile test was added into the model (Figure 4.1). To add stress-strain data into Abaqus, a conversion to true stress and logarithmic plastic strain was required (Equations 4.1 and 4.2) [36].

$$\sigma_{\text{true}} = \sigma_{\text{nom}} \left(1 + \varepsilon_{\text{nom}}\right) \tag{4.1}$$

$$\varepsilon_{\text{ln}}^{\text{plastic}} = \ln(1 + \varepsilon_{\text{nom}}) - \frac{\sigma_{\text{true}}}{E} \tag{4.2}$$

Table 4.2: Relevant mechanical properties.

Material	ρ [kg/m^3]	E [GPa]	ν	σ_y [MPa]
AISI 4130 [1]	7850	205	0.285	805
E190 [2]	7900	190	0.29	210

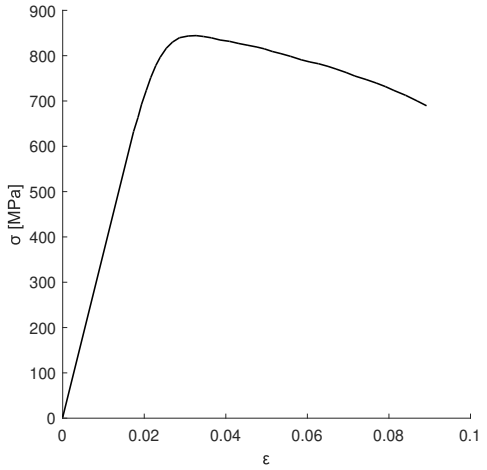

Figure 4.1: Nominal stress-strain curve of the AISI 4130 steel [38].

The geometry was meshed with Abaqus' linear beam elements – B31. Simulations were made with different number of elements, to evaluate convergence, and mesh refinements were made in critical zones.

4.1.2 Results

4.1.2.1 Torsional stiffness

After doing a convergence test, the wheel's vertical displacement remained practically unchanged in the 61.55 to 61.59 mm range (Figure 4.2). Taking into account the most refined case, the vertical displacement is about 61.55 mm. As the track width is 1150 mm, and the applied loads are 5 kN, the torsional stiffness of the frame can be calculated as follows:

$$k_{\mathrm{t}} = \frac{2 \cdot 5000 \cdot 1150/2}{\arctan\left(\frac{61.55}{1150/2}\right)} \approx 53.9 \text{ kNm/rad.} \tag{4.3}$$

When using uprights as Abaqus' default discrete rigid part, a constraint between the uprights and the suspension arms had to be used. After some tests, it was noted that because of the way the constraint was defined, the rotational degrees of freedom of the suspension arms beams were excluded, resulting in no bending. The workaround was to model the uprights as beams, but with a Young's Modulus 10^3 times greater than the

[1] Properties provided by the material supplier.
[2] Properties of E190 taken from [37].

suspension arms modulus, so, when compared with the other materials in the model, they behave as rigid parts (Figure 4.3). This has a noticeable effect on torsional stiffness, as with the rigid suspension arms the achieved vertical displacement was 41.71 mm, which gives a torsional stiffness of 79.4 kNm/rad. Nevertheless, the important thing is to model the suspension arms and uprights the same way in all models under analysis, so that a comparative evaluation of the models can be made, only taking into account the impact of the frame.

Regarding the von Mises stress in Figure 4.4, there are two chassis cross beams with an equivalent stress of around 600 MPa at the endpoints, resulting in a factor of safety of about 1.34. In the case of the suspension arms, a maximum von Mises stress of 660 MPa is obtained, meaning a fracture would occur in this extreme load case. However, in real life application the suspension arms ends are not fixed to the structure, but constrained with rod ends, which results in a lower stress in this area, as there are no reaction moments. Besides that, it is actually preferable to use weaker materials on them, so that in case of extreme loading the failure does not occur on the chassis, which is more difficult to repair.

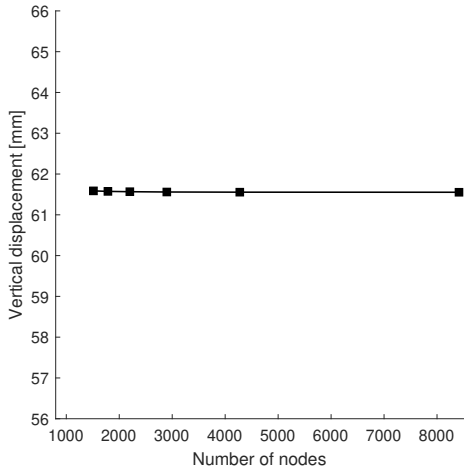

Figure 4.2: Vertical displacement of the wheel depending on the number of nodes, for the steel space frame modelled by beam elements.

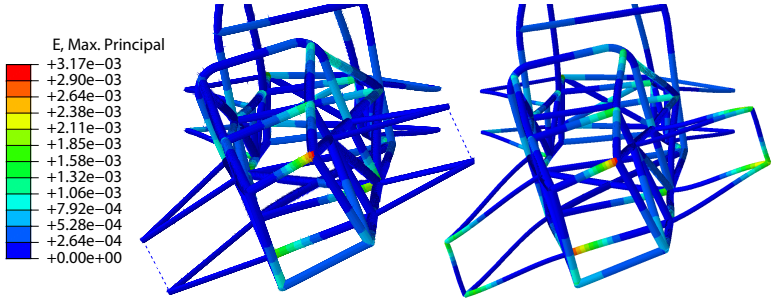

Figure 4.3: Rigid (left) and flexible (right) behaviour of the suspension arms.

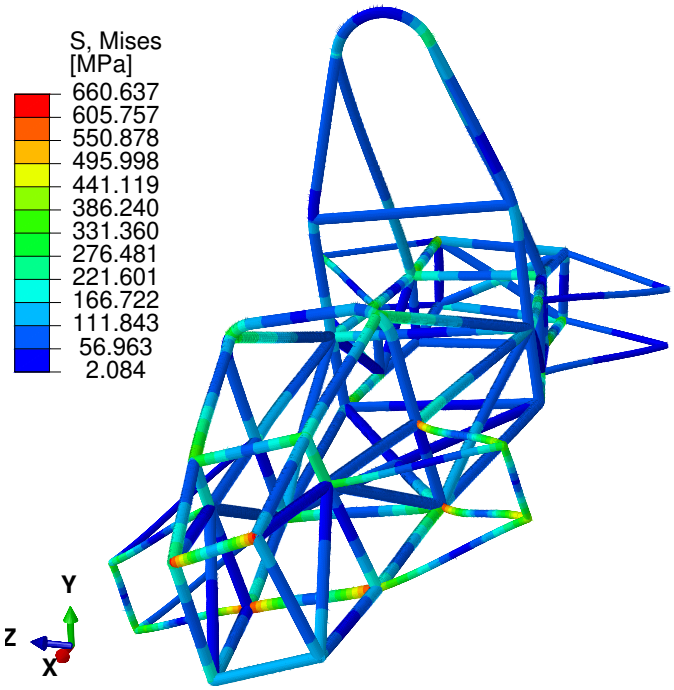

Figure 4.4: Equivalent von Mises stress in torsional stiffness test, for the steel space frame modelled by beam elements.

4.1.2.2 Frontal impact

In Figure 4.5, the evolution of the acceleration as a function of the impact time is shown. The average acceleration along the course of approximately the first 0.07 s was about 27.8 g. Accordingly to [39], a horizontal acceleration of 27.8 g, in this period of time, is not likely to cause serious harm on a person (Figure 4.6). Regarding the peak of 160 g, it will be dangerous for the driver. However, Formula Student cars are required to have a frontal impact attenuator, that will absorb most of the impact energy and provide safe acceleration levels.

Regarding the deformation of the structure – Figure 4.7 – the front of the chassis deformed 250 mm, which will likely not cause any harm to the driver's legs, as in a normal driving position their feet are about 400 mm from there. Regarding the torso, as the front hoop deforms about 222 mm, the steering wheel will not reach the driver. The neck and head are areas that might be compromised, as the main hoop base deforms about 180 mm to the rear, while the top deforms 250 mm to the front, causing the head rest and the shoulder harness mounting bar to rotate forward. It can also be noticed that the engine area has a large deformation. In order to get more accurate results, the analysis of the projected chassis should be made with additional nearly rigid tubes in this region, to replicate the effect of the engine high stiffness.

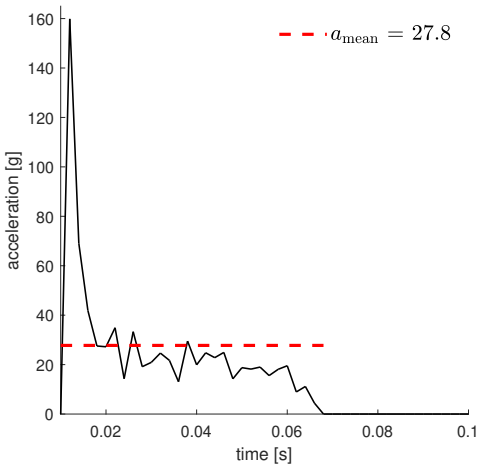

Figure 4.5: Horizontal acceleration over impact time, for the steel space frame modelled by beam elements.

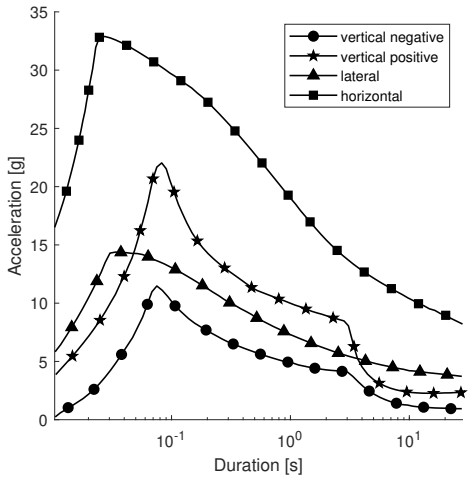

Figure 4.6: Semi-log graph of the limits of tolerance to linear acceleration [39].

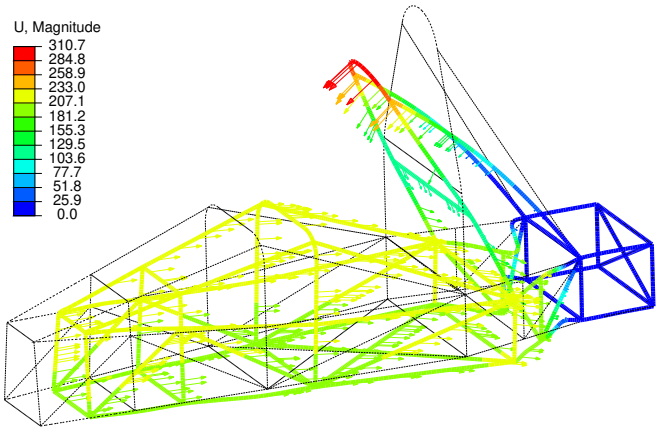

Figure 4.7: Frame shape after frontal impact, for the steel space frame modelled by beam elements.

4.1.2.3 Lateral impact

In Figure 4.8 the acceleration evolution as a function of time is shown, where it can be seen that a peak around 29 g and a mean acceleration of 19.5 g were achieved. As for Figure 4.6, in this impact time the acceleration should be bellow 14 g. However, it should be noted that the lateral impact tubes used in this frame are in accordance with the rules of the competition, regarding their dimensions and position. A possible solution for increasing the driver's safety would be using some energy-absorbing padding on the sides of the seat.

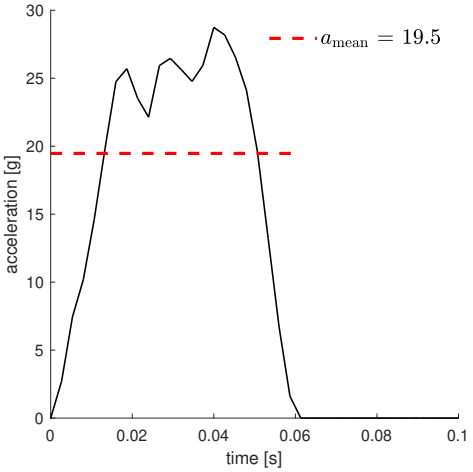

Figure 4.8: Lateral acceleration over impact time, for the steel space frame modelled by beam elements.

Regarding the frame deformation (Figure 4.9), it can be seen that in this situation the lateral impact tubes behave as a three-point bending case. According to the rules, the car should accommodate a driver with a stature up to a 95^{th} percentile male, whose hip width is 405 mm [40]. In this case, the tubes deform around 175 mm towards the

driver, and as the side-to-side distance within this area is about 540 mm (leaving a margin from the pilot to the tubes of about 135 mm), it is likely that they receive some direct impact on the body, so increasing the area moment of inertia (2^{nd} moment of area) of the side impact tubes would be beneficial.

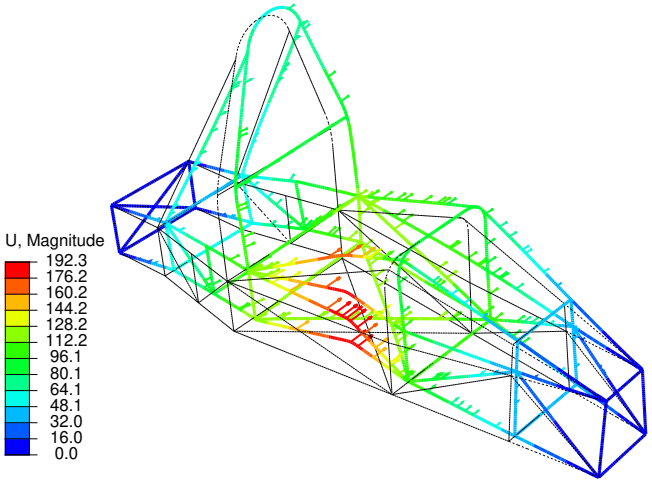

Figure 4.9: Frame shape after lateral impact, for the steel space frame modelled by beam elements.

4.2 Steel space frame with shell elements

The way the tubes are connected at the nodes (Figure 4.10(a)) increases the stiffness in these areas, thus using a model based on a shell mesh with triangular elements can better reproduce the real behaviour of the structure.

Given the complexity of the model, the geometry was imported as surfaces into FEMAP, and then meshed with this software. After hours of user intervention, for manual adjustments to fix some distorted elements, the corrected mesh could be finally exported to Abaqus. In Figure 4.10(b) the details of a representative mesh area are shown.

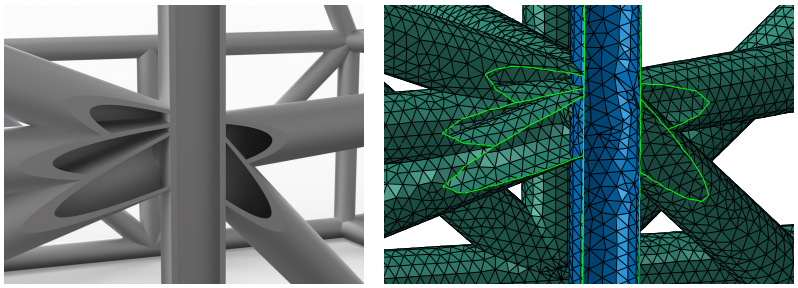

(a) CAD view. (b) Mesh view.

Figure 4.10: Tube coupling detail, after treatment in FEMAP.

As this model is equivalent to the one based on beam-type finite elements, the same materials and profiles listed in Section 4.1.1 were used. Regarding the mesh, Abaqus' linear triangular elements (S3R), with 5 integration points along the thickness were used.

In order to make the comparative analysis between the different models, the suspension arms are modelled with the same materials, profiles and elements. In the tubular beam model, as the geometry is modelled as a wireframe, the different beams, including the suspension arms, are intrinsically connected in the nodes. One the other hand, in the shell model a constraint on 6 degrees of freedom (between the end point of the suspension arms beam and the shell nodes of the chassis) needs to be set up (Figure 4.11).

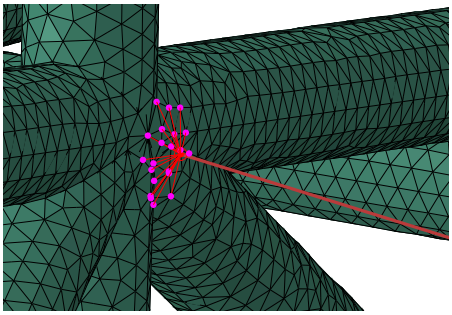

Figure 4.11: Detail of the coupling between the suspension arms beam and the chassis shell.

4.2.1 Results

4.2.1.1 Torsional stiffness

As with the model with beam elements, a brief convergence test was made and, again, the vertical displacement remained practically unchanged (Figure 4.12). With the most refined case, a vertical displacement of about 63.50 mm is obtained, giving a torsional stiffness of around 52.27 kNm/rad. Comparing the results of this model to the previous one, apparently the larger displacement in this model is a contradiction, since the frame nodes are stiffer. However, a possible reason for this 1.95 mm displacement difference is the way the coupling of the suspension arms was made.

While in the beam frame the suspension arms are directly connected to a node, in the shell model they are connected to the edge of the tubes' wall, which is a weaker area, as the load paths are not directly spread over the other tubes. A small deformation on this area has a big impact on the vertical displacement of the wheels. Considering a suspension arm of 450 mm, the 1.95 mm can result of a 0.25° rotation on the attachment area:

$$\arcsin\left(\frac{3.5}{450}\right) \approx 0.25°. \tag{4.4}$$

One of the advantages of using shell elements, instead of beam ones, is the possibility to have results not only along the tubes but also around their surface. In Figure 4.13, one can see that, in fact, there are some areas where the chassis will plastically deform, as in the front bulkhead or at the upper connection of the front up with its braces. The

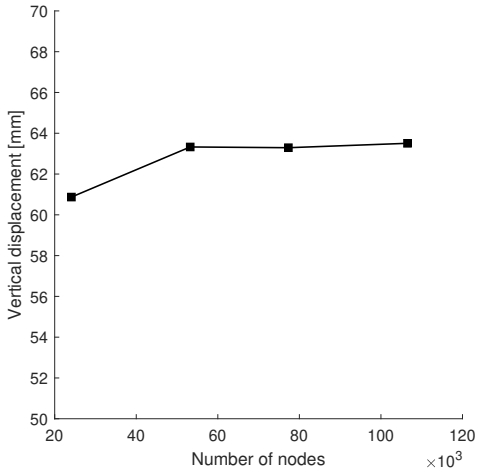

Figure 4.12: Vertical displacement of the wheel centre convergence plot, for the steel space frame modelled with shell elements.

use of gusset plates in this zone might be beneficial in reducing the stress. As can be seen in the lower detail view, the maximum stress of the cross beam is about 500 MPa, instead of the 650 MPa obtained with the beams elements. A possible reason for this is the way the suspension arms coupling was done, reducing load paths to this cross tube.

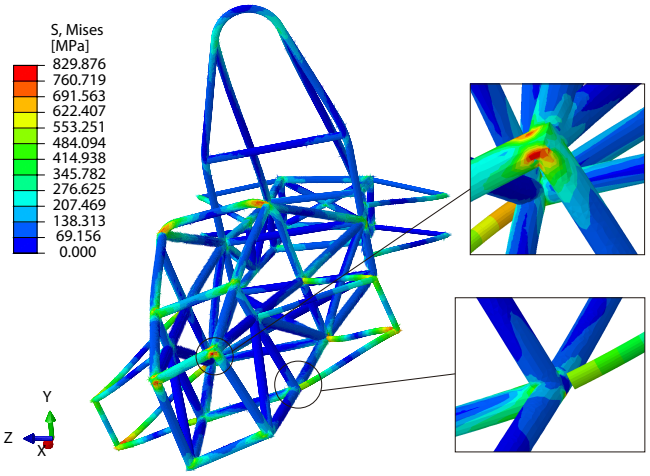

Figure 4.13: Equivalent von Mises stress in torsional stiffness test, for the steel space frame modelled with shell elements.

4.2.1.2 Frontal impact

On the frontal impact test, an average acceleration of 21.1 g was achieved, 6.7 g lower than in the previous model (Figure 4.14). When compared to the Figure 4.6, this gives about 10 g of safety margin. A possible explanation for this lower value is the fact that the connections between the various tubes are all meshed, adding more places where energy can be dissipated. Also, the high number of elements in the mesh (48,844) when compared with the 3,506 elements of the beam model, might give more accurate results.

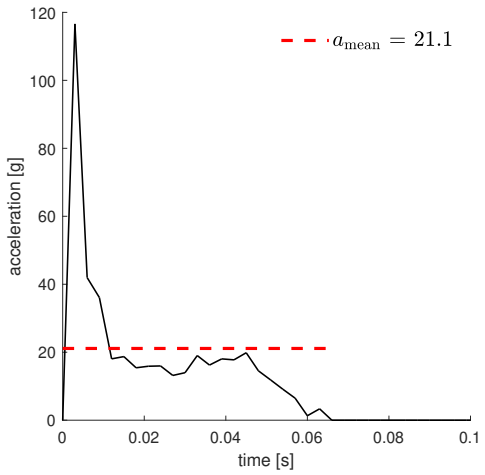

Figure 4.14: Horizontal acceleration over impact time, for the steel space frame modelled with shell elements.

Regarding the frame deformation (Figure 4.15), one can see that the shape of the structure is similar to the one obtained with the beams elements. However, the front of the chassis deformed 155 mm backwards, the front hoop 175 mm and the main hoop base and top deformed 130 and 250 mm, respectively. All these measures are lower than the ones obtained with the beams model. Besides the fact that apparently there is more impact energy being dissipated on the tubes connections, this is also a result of the increased stiffness in these areas. The tubes coupling shown in Figure 4.10(b) act almost as gusset plates, reducing the tubes free length between supports.

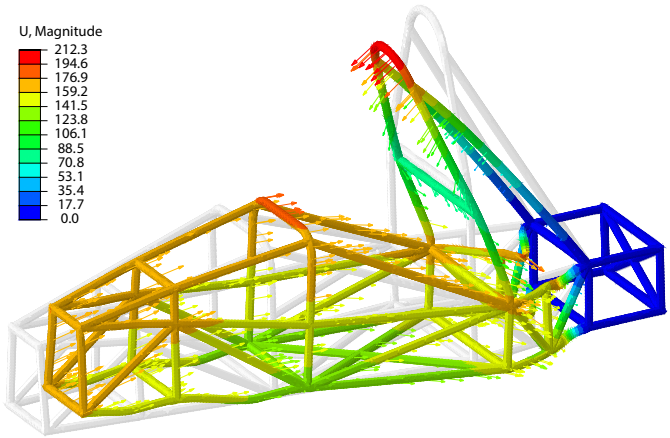

Figure 4.15: Frame shape after frontal impact, for the steel space frame modelled with shell elements.

4.2.1.3 Lateral impact

A peak of around 33 g and a mean acceleration of 22.7 g were achieved, both higher than the 29 g and 19.5 g obtained in the beam model, respectively (Figure 4.16). This seems contradictory to the results obtained on the frontal test, however in this case the initial impact is absorbed by the bending of the side impact tubes. As their free length is reduced by the "gusset plate effect" previously extended upon, their maximum deflection is lower, reducing the impact energy absorbed in this process. The shape of the structure after the impact is shown in Figure 4.17, and one can see that the maximum deflection is around 166 mm, while on the beams model a value of 175 mm was achieved.

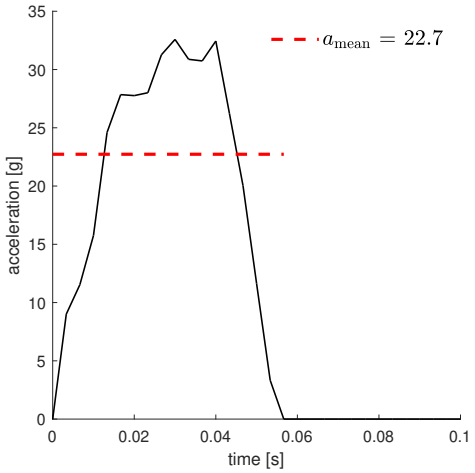

Figure 4.16: Lateral acceleration over impact time, for the steel space frame modelled with shell elements.

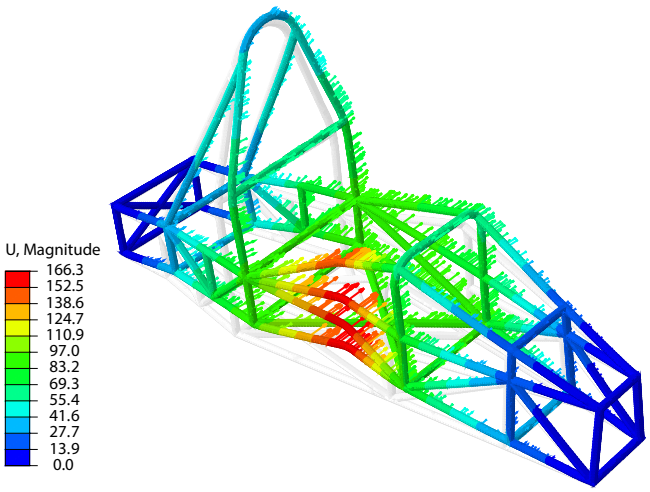

Figure 4.17: Frame shape after lateral impact, for the steel space frame modelled with shell elements.

4.3 Composite space frame

To simulate the composite space frame, the same geometry as the steel frame was used. The tubes were split in such a way that the connections between the carbon elements were made of steel, similar to the chassis of the Divergent's car mentioned in Section 2.2.2 (Figure 4.18). The front hoop and also the main hoop and its braces remained in steel as well, as the competition rules require this.

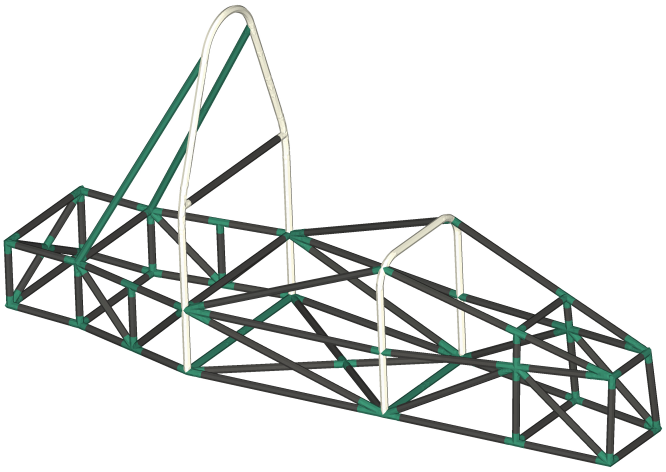

Figure 4.18: Composite space frame geometry.

4.3.1 Materials and profiles

As noted above, the geometry of the structure remained the same as the steel space frame, so the data provided in Tables 4.1 and 4.2 was used. The carbon tubes, represented in black in Figure 4.18, are the only exception. As mentioned in Section 2.8.3.2, the selected

composite tubes are made of five layers arranged in a 0°, 90°, 0°, 90° and 0° layup, where the 0° layers are 300 gsm Toray T700, and the 90° layers are 300 gsm E-Glass. The mechanical properties of these materials are listed in Table 2.4.

In order to assess the damage upon the composite tubes, Hashin damage criteria were used. This damage model is primarily intended for use with fibre-reinforced composite materials, and takes into account four different failure modes: fibre tension, fibre compression, matrix tension, and matrix compression [41]. The longitudinal and transverse strength ,both in traction and compression, as well as the in-plane and out-of-plane shear strengths listed in Table 2.4 were added to the material properties of the model.

4.3.2 Mesh

Due to the complexity of the geometry, FEMAP was used to generate and refine the mesh, and then the model was exported to Abaqus. As with the metal frame with shell elements, the geometry was meshed with 49,918 Abaqus' linear triangular elements (S3R). In the steel areas, 5 integration points along the thickness were used. As for the composite tubes, composite shell sections were created and the layup, with the respective material and orientation, was specified. For each of the 5 layers, 3 integration points along the thickness were used. It should be noted that the geometry was all meshed as one part, so a perfect bonding between the composite tubes and their respective metal connections was considered.

4.3.3 Results

4.3.3.1 Torsional stiffness

After performing the torsional stiffness test, 95.81 mm of vertical wheel centre displacement were obtained, with a mesh of 50170 elements. To get a more accurate result, a convergence test would have to be carried out. However, besides having to make manual adjustments to fix distorted elements, it is also necessary to assign material directions to each individual tube every new mesh, this being a time-consuming task. Nevertheless, the obtained torsional stiffness of 34.82 kNm/rad possibilitates a comparison with the other models.

Regarding the critical points in the metal, plastic deformation occurred at the upper connection of the front up with its braces while the remainder of the frame did not achieve the yield point – Figure 4.19. The maximum von Mises stress was reached in the suspension arms, but as explained before, in real life applications they are connected with rod-ends, reducing these critical values.

As for the critical points in the composite tubes, Hashin's criteria were used. Regarding the fibres, maximum values of 0.629 in compression and 0.156 in tension were reached, which makes sense as the tensile strength of the fibres is higher than the compression one. With respect to the matrix, it was found that the top tube of the front bulkhead had matrix failure, both in tension and compression (Figure 4.20).

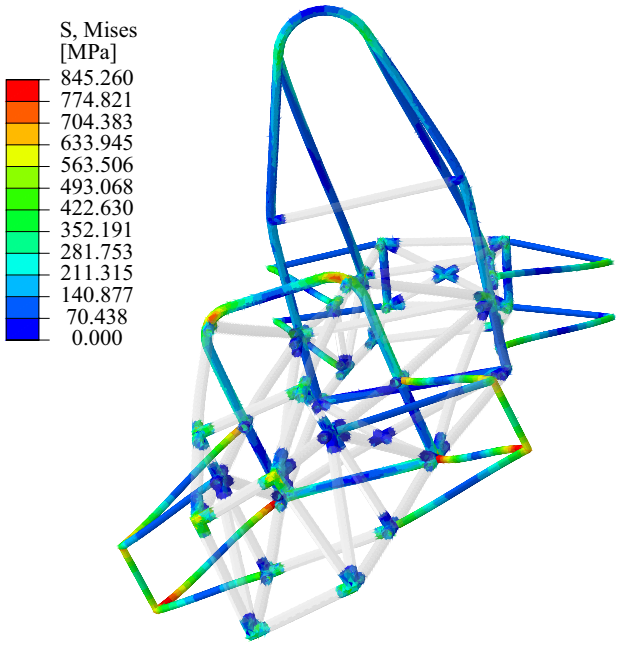

Figure 4.19: Equivalent von Mises stress in torsional stiffness test, for the composite space frame.

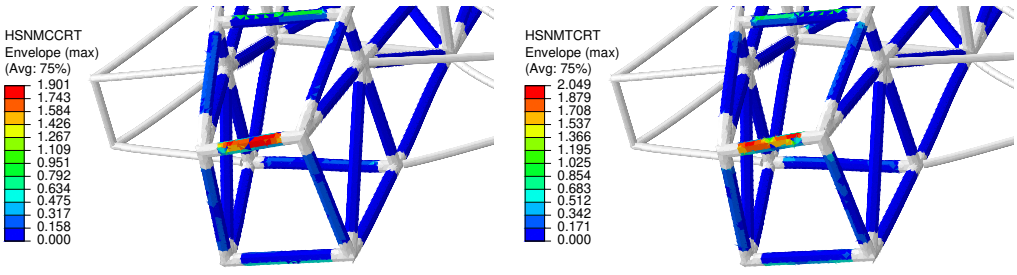

(a) Matrix, compressive failure.

(b) Matrix, tensile failure.

Figure 4.20: Hashin's criteria (maximum value of all layers).

4.3.3.2 Frontal impact

In Figure 4.21 one can see that a peak of 95 g and a mean acceleration of 16.8 g were reached. These values are significantly lower than the 118 g and 21.1 g, respectively, reached with the previous model, demonstrating the good impact absorbing properties of composite materials. Associated with the acceleration reduction, there was an increase in the impact time from 0.065 s to 0.105 s.

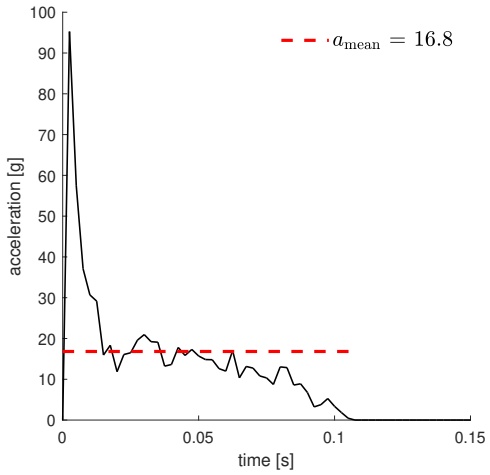

Figure 4.21: Horizontal acceleration over impact time, for the composite space frame.

Regarding the frame deformation (Figure 4.22), it is possible to see that almost all of the impact is absorbed by the frontal part of the structure, contrary to the previous metal frame. It should be noted that in this case failure occurs in 4 tubes, since all Hashin's criteria are far greater than 1, both in tension and compression on the fibres and on the matrix. As a result, large deformation will occur in the driver's legs area, which could compromise their safety. A possible solution for this might be reinforcing the tubes that failed, or replacing them by metal ones.

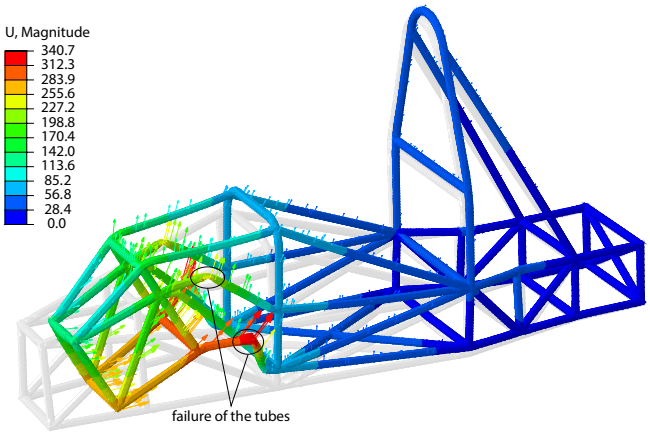

Figure 4.22: Frame shape after frontal impact, for the composite space frame.

4.3.3.3 Lateral impact

In this case, the mean acceleration was 21.8 g, with a peak around 36 g. In comparison with the steel space frame with shell elements, the peak acceleration is 3 g higher. However, as the impact time increased from 0.057 s to 0.068 s, the mean acceleration decreased 0.9 g. As with the frontal impact case, failure of both the matrix and the fibres occurred in the impact zone, though the deformation of the side impact tubes was actually lower than with the metal frame. In Figure 4.24, one can see that the deformation of the side impact tubes was 114 mm. Considering the distance of the pilot to these tubes (mentioned in Section 4.1.2.3), this deformation will not hit the driver's body, by contrast with the metal frame. Comparing the results achieved in the lateral impact to the ones achieved in the frontal one, it can be seen the influence of the tubes behaving better in bending than in compression, as a result of their layup.

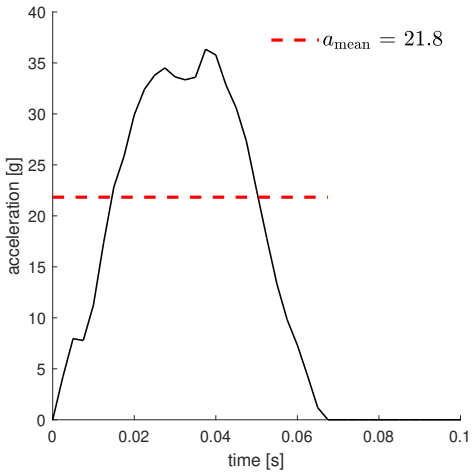

Figure 4.23: Lateral acceleration over impact time, for the composite space frame.

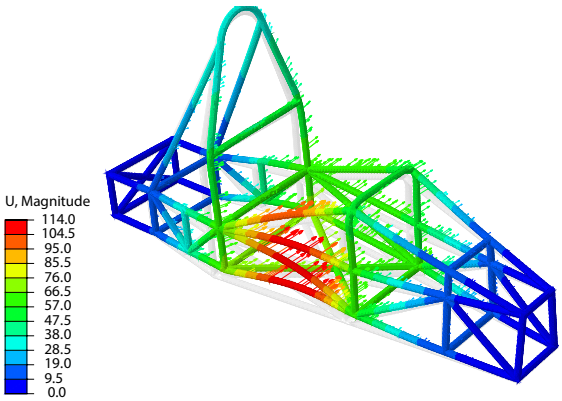

Figure 4.24: Frame shape after lateral impact, for the composite space frame.

4.4 Monocoque chassis

Based on the tubular chassis, a model for the monocoque chassis was designed, as can be seen in Figure 4.25. The model accounts for the same overall shape and dimensions and, as in the previous model, the roll hoops remained as steel tubes. The competition rules state that the roll hops must be mechanically attached to the composite at the top and bottom of both sides of the structure, and the front hoop can be fully laminated to the monocoque [1]. To simplify the FEA model, the hoops were modelled as if they were inserted into the middle of the monocoque wall.

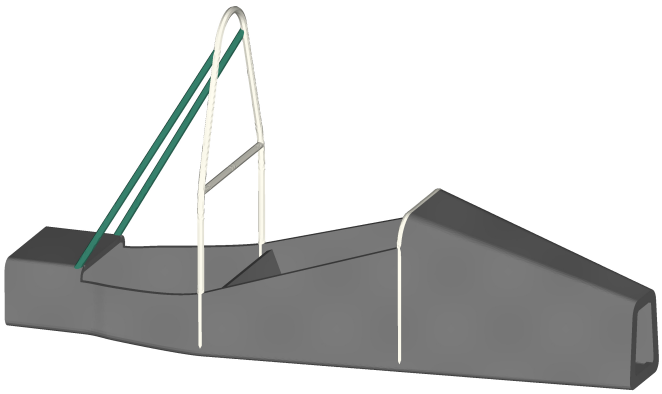

Figure 4.25: Monocoque chassis geometry.

4.4.1 Materials and profiles

Regarding the roll hoops and the main hoop braces, profiles and materials remained the same. For the sandwich structure, the face sheets were made up with the same unidirectional carbon fibre as in the composite space frame case, with 0.1 mm layers in -45°, 0°, +45° and +90° orientations in order to behave more isotropically.

The core material was ROHACELL® 51 WF foam, since it was the only core material whose mechanical properties to fully reproduce its behaviour were found. This type of foam has a cellular material response, and according to Abaqus documentation, the most suitable material model is the crushable foam plasticity model [42]. In Table 4.3 the elastic properties as well as the crushable foam plasticity ones are listed.

Regarding the crushable foam model, Abaqus requires the properties to be in the form of compression yield stress ratio and hydrostatic yield stress ratio. The compression yield stress ratio is the ratio between the compressive and the hydrostatic yield strength (1.04), and the hydrostatic compressive yield stress ratio was considered to be the default value (1.00). Furthermore, to fully reproduce the plastic behaviour, stress-plastic strain was added into Abaqus' crushable foam hardening (Figure 4.26).

4.4.2 Mesh

As in the previous cases, the geometry was meshed in Femap and then imported into Abaqus. The tubes and the sandwich face sheets were meshed with triangular elements. As said in Section 4.4, in order to simplify the model the tubes were directly inserted into

Table 4.3: ROHACELL® 51 WF mechanical properties [43].

Density, ρ [kg/m^3]	52
Young's Modulus, E [MPa]	22
Poisson's ratio, ν	0
Compressive yield strength, σ_c [MPa]	0.85
Hydrostatic compressive yield strength, $\sigma_{Hyd,c}$ [MPa]	0.82

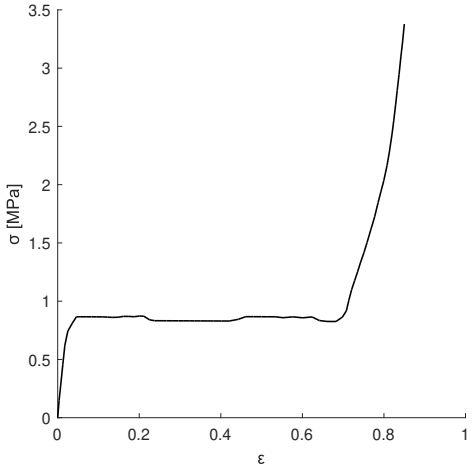

Figure 4.26: ROHACELL® 51 WF stress-strain compression curve [43].

the monocoque, so in the places where the tubes come into contact with the sandwich structure, the nodes of both parts are the same, therefore it is considered that the bond between them is completely rigid. Regarding the core, Abaqus crushable foam model does not work with shell elements, so a mesh consisting of tetrahedral elements had to be used, which severely increased the complexity and the size of the finite element model (Figure 4.27). In total, the model had 124,652 linear triangular elements (S3R), and 429,466 linear tetrahedral elements (C3D4).

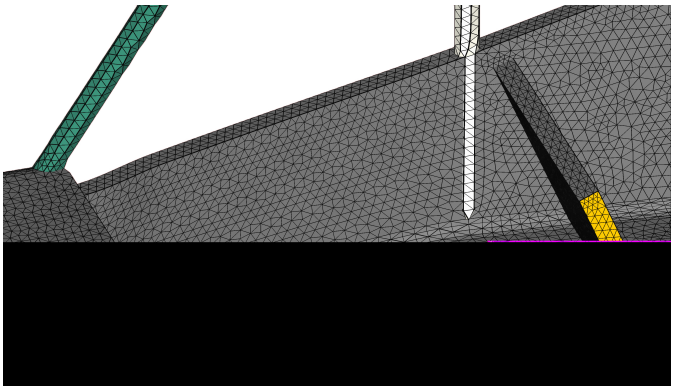

Figure 4.27: Cutaway view of the monocoque meshed geometry.

When running the impact simulations, several problems related to severe distortion with some tetrahedral elements emerged (Figure 4.28). In order to overcome this problem, distortion control, as well as element deletion, was activated, and maximum element degradation was adjusted. However, the simulations continued to abort. The solution was to simplify the geometry, reducing pronounced geometric transitions, and using hexahedral elements with reduced integration. One of the simplifications that was made, was modelling the steel tubes using beam elements coupled to the monocoque walls, in combination with stringer reinforcements.

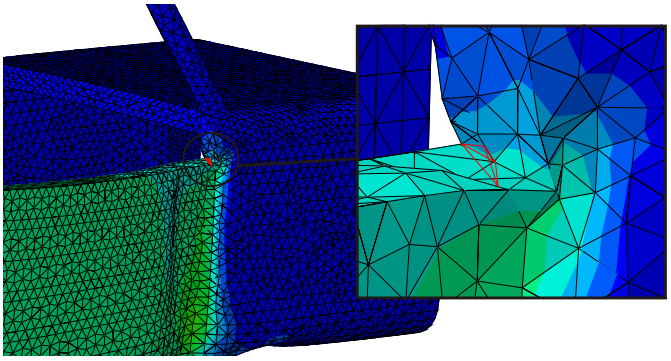

Figure 4.28: Distorted element in the frontal impact case.

4.4.3 Results

4.4.3.1 Torsional stiffness

With the torsional stiffness test, a vertical wheel displacement of 65.08 mm was obtained, resulting in a torsional stiffness of 51.02 kNm/rad. One can see in Figure 4.29, that there is significant deformation on the suspension attachment points. Furthermore, as the shown suspension arms are subject to a downforce, the upper attachment points are in tension and the bottom ones are in compression.

To increase the torsional stiffness, these areas should be reinforced by the replacement of the core with stiffeners of a less compliant material, such as aluminium, plywood or end-grain balsa wood. The core inserts' material and geometry should be choose correctly, not only to withstand the loads, but also to prevent high peak stresses around it [8].

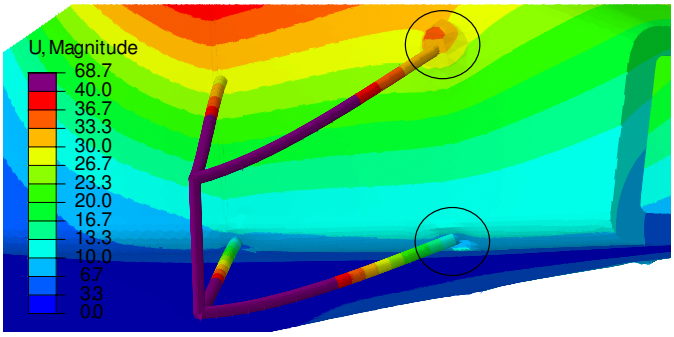

Figure 4.29: Deformation detail on the suspension arms attachments points.

Regarding the hydrostatic stresses on the core foam (Figure 4.30(a)), maximum values of around 0.3 MPa are reached, which is lower than the yield strength. In the upper suspension attachment point of the front right suspension, there is a maximum tensile stress of around 0.77 MPa, while in the left one there is a compressive stress of around 0.78 MPa. Although this is not a problem for compression, since the yield strength is not reached, tensile stresses should be lower, as the core shoud mainly be loaded in compression. Again, the use of inserts in the suspension attachment points is recommended, as well as using backing plates.

There are also stress concentrations in geometric transition zones, such as the coupling of the main hoop bracing supports with the monocoque, or the transition from the monocoque's lateral walls to the rear bulkhead. In the areas where the tubes are attached, core inserts and backing plates should also be used, and the geometric transitions should be smoothed.

As for the von Mises stress on the steel tubes (Figure 4.30(b)), there is a maximum value of about 700 MPa on the front hoop bend, meaning the material will not plastically deform. As in the previous cases, there are high stress values in the suspension arms that will be reduced in a real life application.

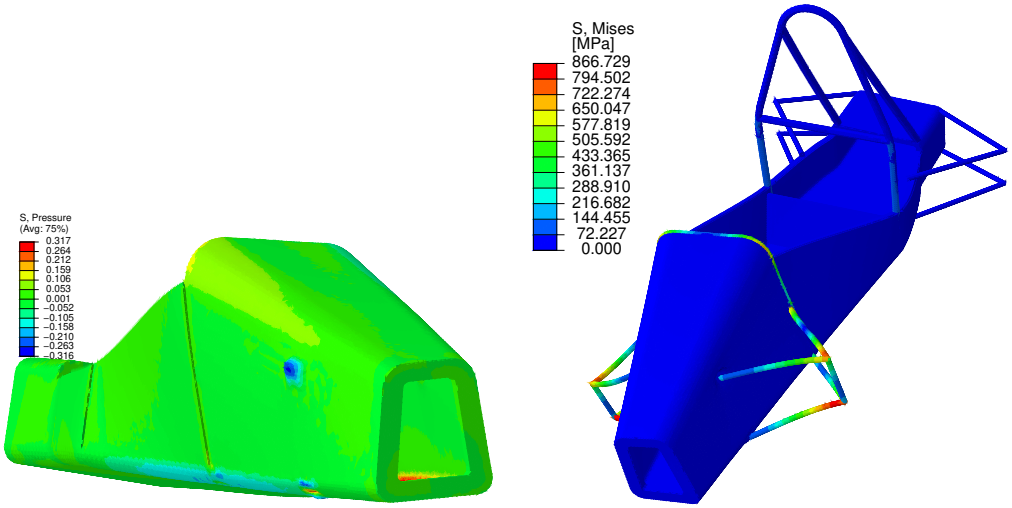

(a) Hydrostatic stress in the core. (b) Equivalent von Mises stress.

Figure 4.30: Stresses in torsional stiffness test.

In terms of composite failure, and regarding the fibres, the critical areas are the same areas as for the core (Figure 4.31(a)), and a maximum value of 0.6 in tension and 2.5 in compression were obtained. Improving these areas with the previously mentioned measures should solve this problem.

In regard to matrix failure, maximum values of 153.9 in tension and 7.5 in compression were achieved. For the compressive criterion, the critical zones are the same, but for the tensile one there are additional critical zones, mainly on the transition on the front hoop area – Figure 4.31(b). As the obtained value is high, these areas should have a smoother geometric transition, and also an increase on the number of plies.

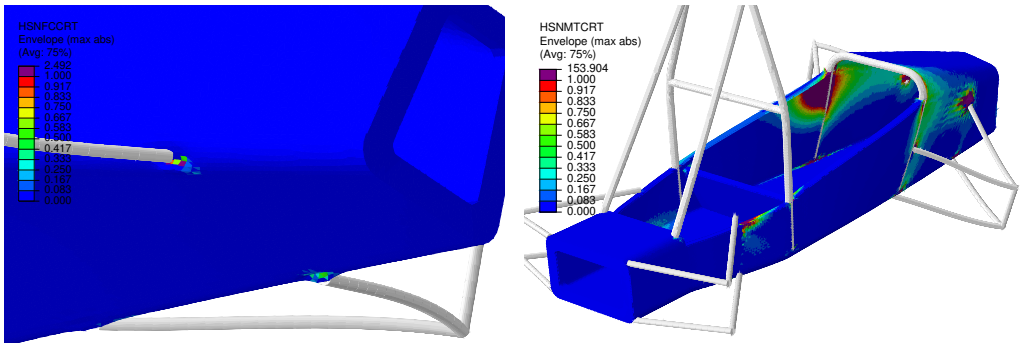

(a) Fibres, compressive failure. (b) Matrix, tensile failure.

Figure 4.31: Hashin's criteria (maximum value of all layers).

4.4.3.2 Frontal impact

Despite all the adjustments that were made (in particular to the mesh size and distortion control), it was not possible to successfully conclude the analyses. The simulation that reached further in time (around $3.26 \cdot 10^{-3}$ seconds) was the one with a mesh of 356,000 elements, and a distortion control length ratio of 0.2.

In this amount of time, a maximum of about 30 g was reached (Figure 4.32). Comparing with the acceleration curves of the other models, it is expected that from around this point the acceleration will gradually drop to zero. However, as the shape of the chassis is quite different from the previous space frames, only a full simulation can confirm this.

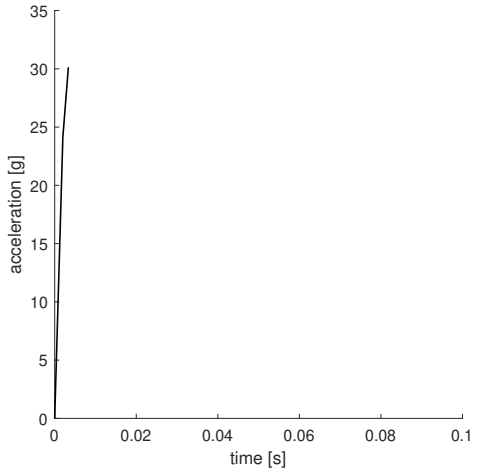

Figure 4.32: Horizontal acceleration over impact time, for the monocoque chassis.

In Figure 4.33, one can see that until the moment of abortion, the main section that suffered deformation was the frontal one, with a displacement of about 36 mm. In this case, the failure of the simulation was due to a heavily distorted element in this area (Figure 4.34).

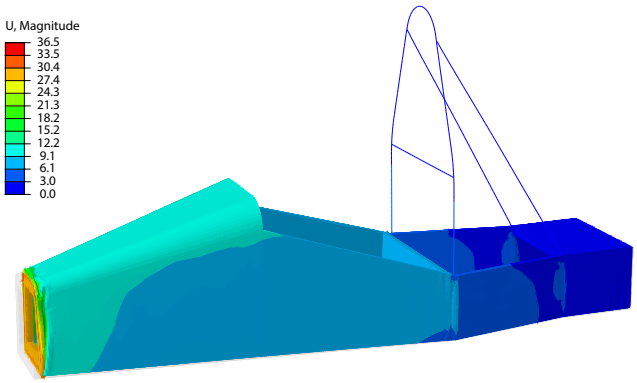

Figure 4.33: Shape of the structure at $3.26 \cdot 10^{-3}$ seconds.

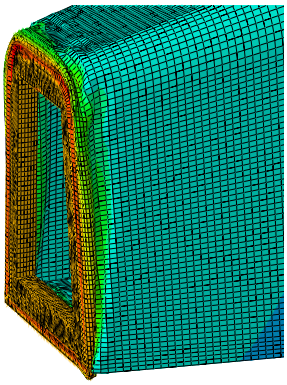

Figure 4.34: Detail of the front section.

4.4.3.3 Lateral impact

The lateral impact test resulted in a mean acceleration of 19.8 g and a peak of around 35 g (Figure 4.35). These values are lower than the previous models, and the impact time was also higher (0.0698 s), which shows the good energy absorption capacities of this type of composite structures. However, the average acceleration remains higher than the acceleration tolerance (about 14 g, for this impact time).

As in this model hexahedral elements with reduced integration and distortion control were used, it is important to assess the energy generated by the hourglass phenomenon (ALLAE) and the distortion control (ALLDC) relatively to the internal energy (ALLIE). In Figure 4.36, it can be seen that the energy associated with the hourglass is significantly lower than the total energy. Using a finer mesh, for instance, might be useful to further reduce this effect. Regarding the energy introduced by the distortion control, it can be seen that its effect is insignificant.

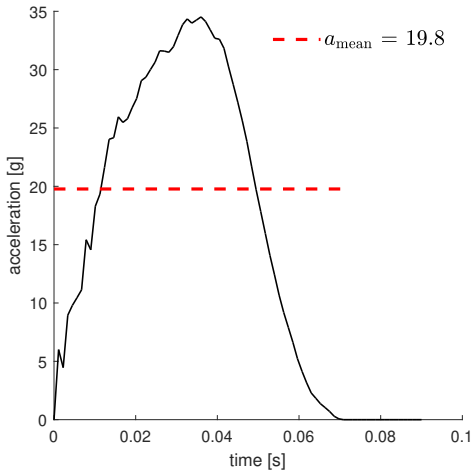

Figure 4.35: Lateral acceleration over impact time, for the monocoque chassis.

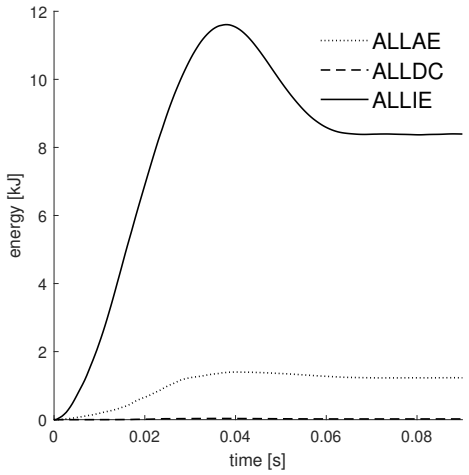

Figure 4.36: Energy history over impact time (ALLAE – "artificial" strain energy, ALLDC – energy dissipated by distortion control, ALLIE – total strain energy).

In Figure 4.37, one can see that deformation mainly occurs on the impacted area, and the deformation of the remaining structure was nearly zero, by contrast with the previous models where all the structure deforms. In the figure, a maximum deformation of 117.8 mm is shown. However, as in this case the impacted zone is basically the only area being deformed, and the rest of the structure (including the driver's area) remains in the same place, during the impact a maximum penetration on the driver's region of around 205 mm is achieved. With such a large deformation, the driver will be hit, so a reinforcement of the side impact structure should be done.

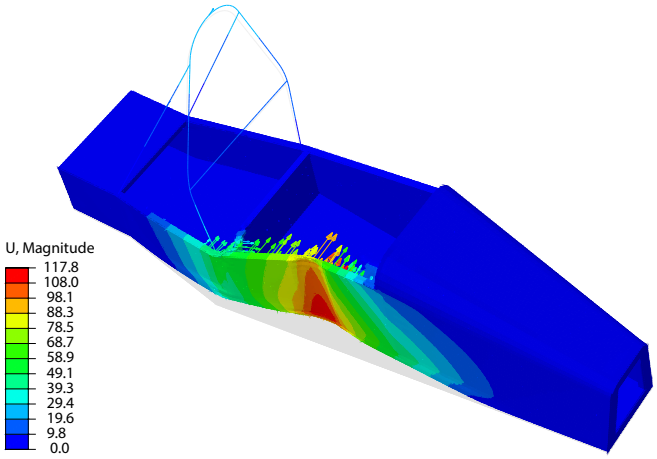

Figure 4.37: Frame shape after lateral impact.

Chapter 5

Model comparison

In Table 5.1 a summary of the results of the previous sections is shown. Regarding the torsional stiffness, the metal space frame has the highest value (52.27 kNm/rad), while the composite space frame and the monocoque chassis have 34.82 kNm/rad and 51.02 kNm/rad, respectively. However, the weight of the metal space frame (38.4 kg) is almost twice as much as the other two chassis (20.2 kg in the composite space frame and 18.2 kg in the monocoque).

Looking at the specific torsional stiffness, one can see that due to its high weight, the steel space frame has the lowest specific torsional stiffness. By contrast, the monocoque chassis has the highest value (2.80 kNm/(kg $\cdot$ rad)).

It should be noted that for a combustion vehicle, instead of a monocoque chassis the most appropriate solution is the hybrid chassis, as the heat dissipation in the engine compartment is favoured and the powertrain fixation and maintenance is easier. If the rear of the monocoque under analysis was replaced by the rear of the steel space frame, its weight would increase about 5.97 kg, leading to a decrease in specific stiffness to 2.11 kNm/(kg $\cdot$ rad) (considering that it would maintain the same torsional stiffness).

Table 5.1: Summary of the achieved results.

Chassis type	Torsional stiffness [kNm/rad]	Mass [kg]	Specific stiffness [kNm/(kg $\cdot$ rad)]
Steel space frame	52.27	38.4	1.36
Composite space frame	34.82	20.2	1.72
Monocoque	51.02	18.2	2.80

Because it was not possible to complete the frontal impact simulations of the monocoque chassis, its scoring was done in an empiric and qualitative way. For the ease of manufacture, factors such as the number of machines and expected labour hours were taken into account. As to cost estimation, a budget estimation was done taking into account the main materials of the structures. In Appendix B, the scoring process is

explained in more detail.

To obtain a global score for each chassis, the different parameters being considered were scaled, with the best value, in each property, being 10 points. By doing this, different properties with different dimensions could be combined, with the respective weighting factor, to obtain a total score.

In Table 5.2 the obtained results are shown. One can see that the steel and the composite space frames obtained the same total score. In the area associated with the vehicle's performance (specific stiffness and driver safety), the composite space frame showed better results. On the other hand, the steel space frame got better results due to a slightly easier manufacture process, and also due to a much lower materials cost.

At the end of this work, a problem regarding the definition of the material properties of the monocoque chassis was detected. When the decision was made as to which chassis was the most appropriate to develop, the results regarding the monocoque were worse in terms of torsional stiffness, giving a total score of 7.5. Therefore, the choice was made between the steel and the composite space frame chassis. As the composite space frame would be something innovative to be presented in the competition, and the impact of the materials' price could be mitigated through sponsorships, this was the selected option to be developed.

Table 5.2: Concept scoring of the different solutions.

Chassis type	Torsional stiffness (30%)	Mass (30%)	Driver safety (20%)	Ease of manufacture (15%)	Material cost (5%)	Score
Steel space frame	10	4.7	8.7	10	10	8.2
Composite space frame	6.7	9.0	10	8.8	2.8	8.2
Monocoque	9.8	10	8.2	5.0	4.1	8.5

Part III

Final solution

Chapter 6

Development of the new solution

6.1 Chassis improvement

The team's development should be continuous and the problems of the current car should be identified, so that each new car is better than the previous one. Throughout the construction of the first car, several issues on the chassis that need to be improved or corrected were detected:

- **Cockpit internal cross section:** some last-minute adjustments were made to the angle of some tubes prior to its construction, in order to ease the tubes' positioning. As a result, the cross section was reduced not allowing the rules' cockpit internal cross section template to reach the initial intended position.
- **Hoops' height:** although some driver templates were used to assess the chassis dimensions, seeing the actual frame after being built, provides a better perspective on some aspects. One of these aspects was the hoops' height, which was oversized.
- **Shoulder harness mounting bar:** the shoulder harness bar should not be straight. Instead, it should be bent backwards, allowing the driver to have a more reclined driving position, lowering the overall centre of mass height and also making it possible to reduce the hoops' height further.
- **Main hoop bracing tubes:** the tubes positioning should be improved, as the current ones are at the limit of what is allowed by the competition rules, which may cause problems in the technical scrutineering phase.
- **Front bulkhead:** the front bulkhead's width should be increased, in order to allow the use of shorter impact attenuators while maintaining the same volume. Besides that, it will allow the use of the competition's standard impact attenuator, in case of problems with the impact attenuator developed by the team.
- **Mounting points:** ideally, the chassis should be designed in an "outside-in" approach, meaning the suspension department gives the exact position of the suspension mounting points, and then the chassis is designed from there. On the current chassis, there are some suspension points that are not located at the chassis nodes, leading to an increase of the compliance of the system. Regarding the engine and

differential mounting points, the chassis tubes should also be adjusted, in order to minimise unnecessary weight and allow the mounting to the frame nodes.

- **Material and profiles availability:** this is one important aspect that should be taken into consideration when designing the chassis, as sometimes it is hard to find a supplier that can provide the materials with the intended properties and dimensions. The current team's chassis was initially designed taking into consideration the minimal material requirements of the rules, and afterwards, adjustments had to be made as the desired profiles were not found on the market, resulting in an increase of around 8 kg of weight.

6.2 Design process

Firstly, the location of the suspension attachments were set. Afterwards, two extruded solids, corresponding to the cross section and cockpit opening templates (Figure A.1, Appendix A), were done. As the size of the templates gives the minimum dimensions that the chassis must have, a 25 mm margin was added. Besides these templates, the 95^{th} percentile male template was also drawn, with the intended driver position. This allowed to establish the height of the hoops and the length of the front section of the chassis.

Formula Student has a set of rules regarding the hoops bracing, and also the tubes placement on the side impact structure, between the main hoop and its bracing supports, and between the front hoop and the front bulkhead. After ensuring the different rules were respected, some doubts arose regarding the placement of the additional chassis elements.

6.3 Assessment of the positioning of the additional tubes

In order to evaluate which solution would be more beneficial, in regard to torsional stiffness, various possible layouts were simulated in Abaqus. Although the solution in development was a tubular composite chassis, because of the composite material it would be necessary to use shell elements, meaning that the FEA model would have to be set and adjusted in FEMAP, and then exported to Abaqus, which would be a very time-consuming process.

To simplify the process, the impact of the placement of the tubes on the torsional stiffness was assessed using the same properties that were used with the steel space frame that was previously analysed, and using beam elements. Although different values would be obtained by performing the simulations with the carbon composite tubes, it is possible to have a general idea of the impact of the tubes' placement.

In Figure 6.1 the tubes under analysis are shown in blue. Regarding the side impact area, it was considered whether it would be more advantageous to have a tube connecting the front hoop and the middle of the side impact structure, or to connect directly the two hoops (options 1 and 2).

As to the area between the front hoop and the front bulkhead, three layouts were assessed: opposing diagonal tubes (option 3), diagonal cross tubes (option 4), or transverse tubes (option 5). It was also assessed whether it would be more advantageous to have a diagonal element or two diagonal cross tubes in the bulkheads (options 6, 7, 8, 9,

10 and 11). The same was done on the main hoop area behind the driver's seat (options 13 and 14), and additionally a transverse tube was also taken into account (option 12).

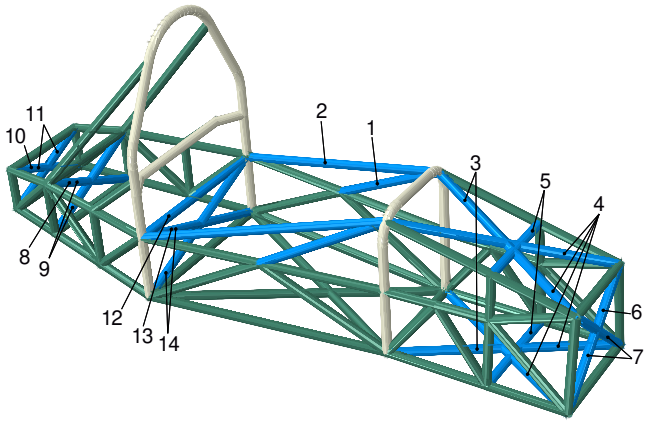

Figure 6.1: Different tubes placements under analysis.

6.3.1 Results

The results for the different scenarios are listed in Table 6.1. Regarding the connection between the hoops, option 2 is the best one, as the torsional stiffness and the specific torsional stiffness reach higher values.

Between options 3, 4 and 5, there is a large difference between the transverse tube (option 5) and the ones with diagonal elements. As can be seen, in this case having diagonal-crossed elements leads to a slightly increase of torsional stiffness (52.31 kNm/rad versus 51.05 kNm/rad in the single diagonal tube), but this effect is outweighed by the increase of weight, leading to a lower specific stiffness. It should be noted that using only one diagonal tube leads to an asymmetrical chassis, so the absolute vertical displacement on the front wheels is slightly different: 65.04 mm on the left side and 65.23 mm on the right one. This results in a torsional stiffness of 51.05 kNm/rad if the displacement is measured on the left side, and 50.90 if it is on the right side, which is an insignificant difference.

Regarding the bulkheads, in all situations the difference in specific stiffness is negligible, so the lighter option was chosen. As for the main hoop zone, option 14 is the best one, as the torsional specific stiffness is higher than the other two options.

6.4 Selection of the profiles

After the position of the tubes was established, it was necessary to pick the most optimal tube profiles to use. For the tubes joints, 4130 was considered, as it provides a higher factor of safety than CDS tube, and because sections with the intended minimum material requirements were founded at a reasonable price.

To establish the profiles to be used in the new solution, a list of the available 4130 tubes was made, and then, the minimum material requirements (indicated in Table 2.3) and the linear density were taken into account (Table 6.2). In the last three columns, the

Table 6.1: Impact of the tubes' layout on torsional stiffness, mass and specific stiffness.

Option	Torsional stiffness [kNm/rad]	Mass [kg]	Specific stiffness [kNm/kg · rad]
Reference	36.01	40.0	0.90
1	43.93	41.1	1.07
2	46.69	41.9	1.11
3	51.05	41.6	1.23
4	52.31	43.1	1.21
5	39.67	40.8	0.97
6	36.87	40.5	0.91
7	37.43	41.0	0.91
8	36.78	40.5	0.91
9	37.10	41.0	0.90
10	36.68	40.4	0.91
11	37.25	40.8	0.91
12	36.58	40.6	0.90
13	36.65	40.7	0.90
14	37.95	41.4	0.92

profiles that fulfil the rules (minimum thickness, cross sectional area and area moment of inertia) are marked. The selected profiles were the ones that had the lower linear density, in order to reduce the weight of the chassis: 30 x 2 mm for group 1, 28 x 1.5 mm for 2 and 25 x 1.5 mm for 3.

Table 6.2: Profile selection.

Dimensions [mm] [44]	Area [mm^2]	Area moment of inertia [mm^4]	Linear density [kg/m]	G_1[1]	G_2[2]	G_3[3]
$\varnothing_{ext}$ 25 x 1.5	110.7	7675.7	0.88			✓
$\varnothing_{ext}$ 25 x 2	144.5	9628.2	1.13		✓	✓
$\varnothing_{ext}$ 28 x 1.5	124.9	10997.1	0.98		✓	✓
$\varnothing_{ext}$ 30 x 1.5	134.3	13673.7	1.05		✓	✓
$\varnothing_{ext}$ 30 x 2	175.9	17329.0	1.40	✓	✓	✓
$\varnothing_{ext}$ 35 x 1.5	157.9	22189.9	1.24		✓	✓
$\varnothing_{ext}$ 35 x 2	207.3	28328.5	1.63	✓	✓	✓

Carbon tubes were selected from [27], and they were chosen so that their inner

[1]Hoops and shoulder harness bar.
[2]Side impact structure, front bulkhead, roll hoops bracing and driver restraint harness attachment.
[3]Front bulkhead support and main hoop bracing supports.

diameter was greater than the outer diameter of the corresponding steel tube, to allow the fitting. Therefore, woven carbon tubes of 31.3 x 1.4 mm and 29.3 x 1.4 mm were selected for groups 2 and 3 (since the rules require group 1 to be metal).

6.5 First iteration analysis

A torsional stiffness simulation, as well as impact simulations, was performed to assess which areas of the new chassis needed improvement.

6.5.1 Torsional stiffness

In the torsional stiffness simulation, a vertical displacement of the wheel of 48.66 mm was obtained, resulting in a torsional stiffness of 68.11 kNm/rad. This is slightly below the target interval defined in the graphic of Figure 2.13 (75 to 165 kNm/rad). As this chassis has a mass of 25.1 kg, this results in a specific stiffness of 2.72 kNm/(kg · rad), a value 58% higher than the previous composite frame chassis, and almost as high as the monocoque one.

The use of gusset plates in some zones, for instance, could improve the torsional stiffness, but the weight would also increase. Instead, the suspension department should better review the choice of the suspension arms tubes, in particular in terms of the chosen profile. Performing the torsional test with rigid suspension arms results in a torsional stiffness of 161.32 kNm/rad, which is above the competition average, and close to the upper limit of the optimal interval.

Regarding the critical points in the frame, the maximum von Mises stress was 787 MPa, so the steel tubes will not plastically deform. As for the carbon tubes, using Hashin's criteria, the fibres reach a value of 0.094 in tension and 0.297 in compression. However, in the matrix failure will occur, both in tension (1.147) and in compression (1.131), in the two lower tubes behind the main hoop (Figure 6.2). These tubes could be replaced by the corresponding metal ones, but in the real life application, the maximum vertical load in the wheel will be around 2.8 times lower, and as the engine is located in this area, it will sustain part of the stress.

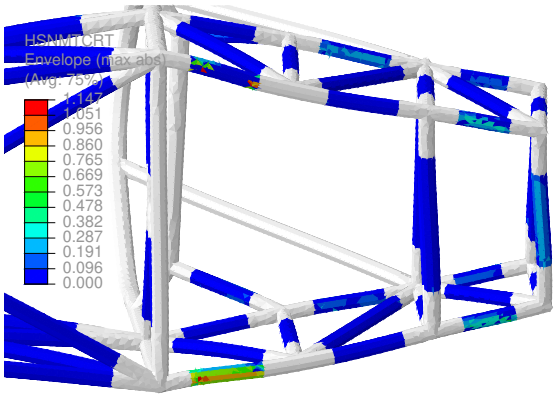

Figure 6.2: Tensile matrix failure, bottom view.

6.5.2 Impact simulations

Some problems arose while doing the frontal impact simulation. Firstly, the rear section of the chassis suffered large deformation (Figure 6.3). To better simulate the real behaviour, some near-rigid beam elements were added to this area, by coupling constraints, to emulate the effect of the engine's stiffness.

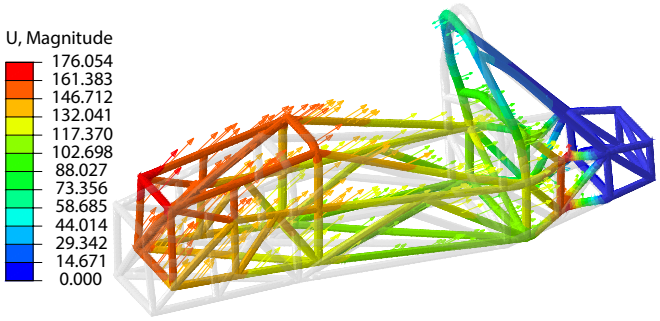

Figure 6.3: Shape of the structure after impact, without the effect of the stiffness of the engine.

Figure 6.4 shows the maximum deformation of the chassis in the frontal impact, after the rigid tubes were added. One can see the effect of the diagonal cross tubes 1 and 2, mainly on sections A, B and C. Tube 1 transfers part of the load to the left side of the chassis, so the overloading leads to major deformation of section A. Furthermore, part of that transferred load is also carried through the diagonal tube under the driver's seat, causing greater deformation in section B. The same principle applies to C, due to the effect of tube number 2. To reduce this effect, it was decided to use two diagonal crossed tubes

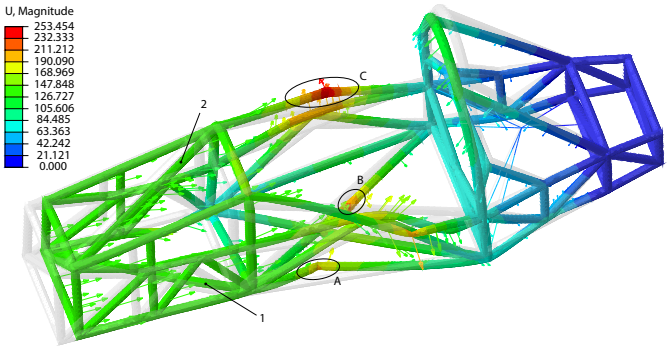

Figure 6.4: Shape of the strucutre (maximum deformation, at t = $3.8 \cdot 10^{-2}$ s), with a deformation scale factor of 0.5.

Chapter 7

Analysis of the final design

7.1 Final design

The final version of the chassis, after the necessary modifications were made and with the several sections marked in different colours, is shown in Figure 7.1. Figure 7.2 shows the differences to the previous steel space frame.

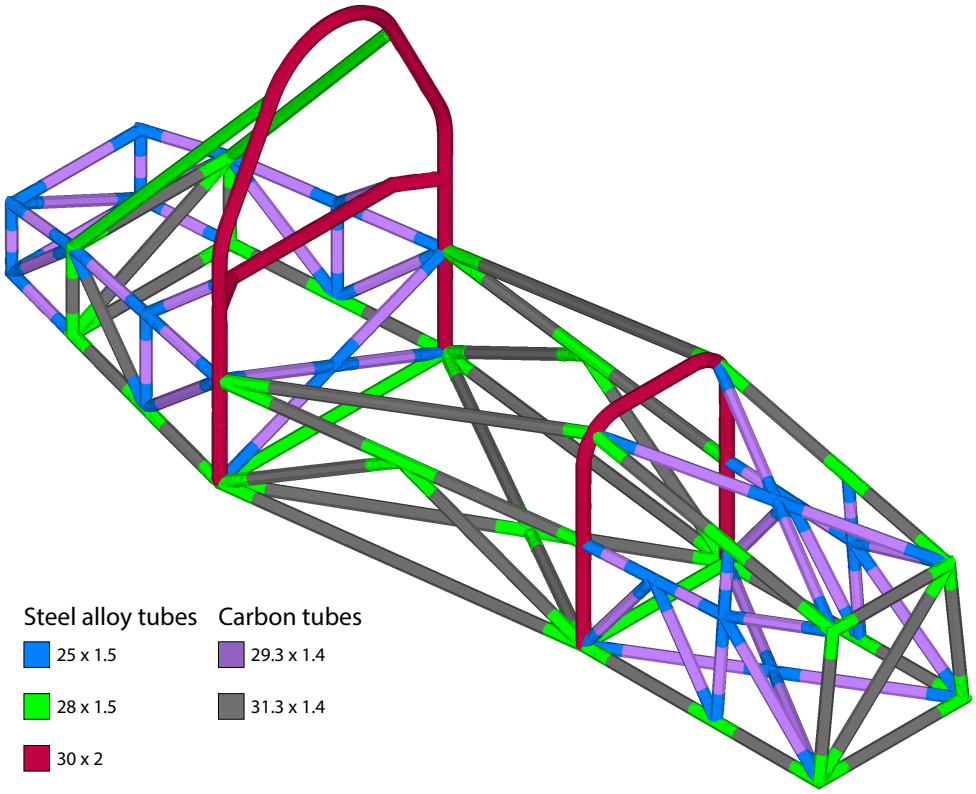

Figure 7.1: Geometry and profiles used in the new chassis.

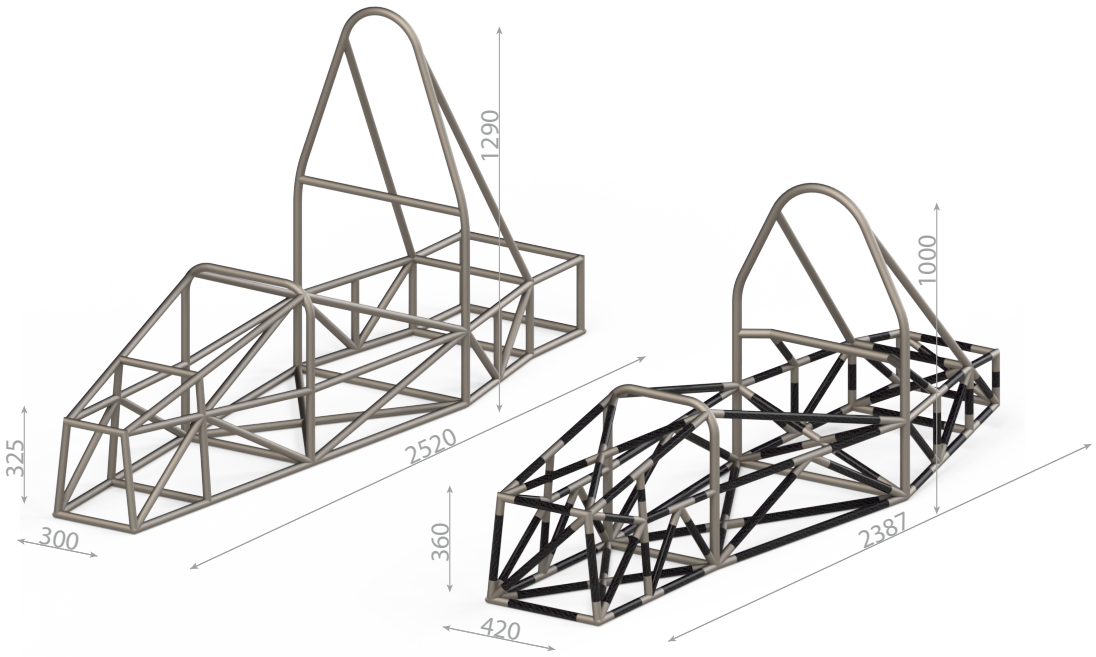

Figure 7.2: Final solution of the chassis (right), compared to the previous steel space frame (left).

7.2 Torsional stiffness

To ensure the quality of the proposed solution, some numerical simulations were performed. In the torsional stiffness one, a vertical wheel displacement of 49.93 mm was obtained, giving a torsional stiffness of 70.61 kNm/rad. Therefore, the addition of the crossed diagonal tubes lead to an increase of about 2.5 kNm/rad. Additionally, the increase of weight to 25.9 kg resulted in a negligible increase of 0.01 kNm/(kg · rad) (2.73 kNm/(kg · rad)) .

Regarding the von Mises stress on the metal joints, one can see that the maximum value is 645 MPa, which gives a factor of safety of around 1.25, for this extreme load scenario (Figure 7.3). One of the areas where there is a higher stress value is in the junction of the main hoop with the side impact structure, since this area is essentially a load path between the front and the rear sections.

Hashin's criteria indicate that failure does not occur in the fibres, as maximums of 0.094 for tensile failure and 0.282 for compressive failure were achieved. For the matrix, values of 1.126 for tensile failure and 1.106 for compressive failure were obtained in the same critical area that was identified in the first iteration analysis. However, it should be noted that this extreme load scenario (two opposite loads of 5,000 N) is well above the single 3,530 N that arises in the combined, and unlikely, event of cornering with a lateral acceleration of 2.2 g, combined with full braking and a 100 mm deep hole. Performing the simulation with two 4,000 N loads, does not result in failure: 0.720 is achieved in tension, and 0.707 in compression (Figure 7.4).

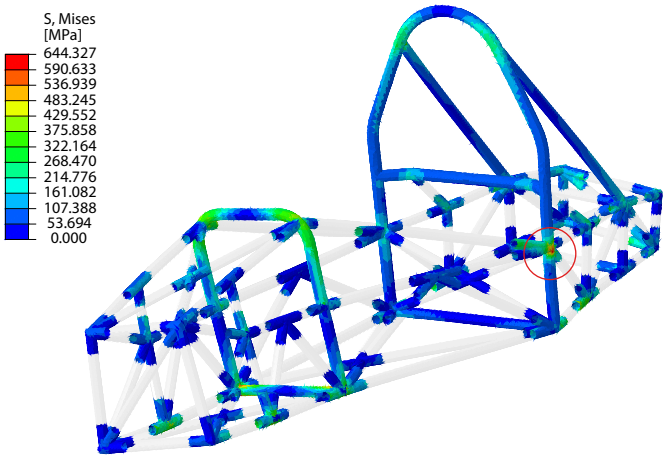

Figure 7.3: Equivalent von Mises stress in torsional stiffness test.

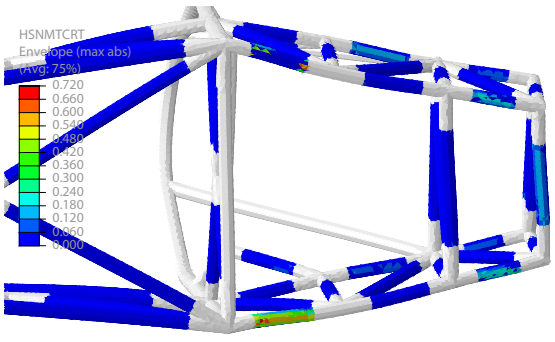

Figure 7.4: Tensile matrix failure criterion, with two opposite 4000 N loads.

7.3 Frontal impact

In the frontal impact simulation, there was a mean acceleration of 29.6 g, and a peak of about 165 g (Figure 7.5). These values are higher than the ones obtained in the previous frames. One of the reasons for this is the inclusion of the rigid tubes to emulate the engine's stiffness, since the first iteration of the chassis resulted in a peak of 100 g, and a mean acceleration of 28.4 without the rigid tubes, and 34.1 g and 160 g with them. Nevertheless, a mean acceleration of 29.6 g will not cause serious harm to the driver and, furthermore, the impact attenuator will significantly reduce it.

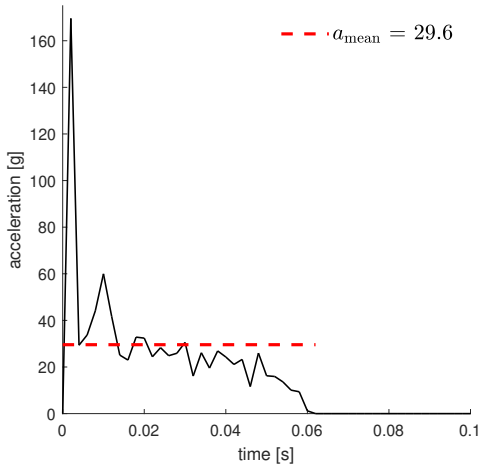

Figure 7.5: Horizontal acceleration over impact time.

In Figure 7.6, one can see that adding the two diagonal cross tubes improved the response of the chassis to deformation. All the tubes of the side impact structure bent outwards, increasing the driver's safety.

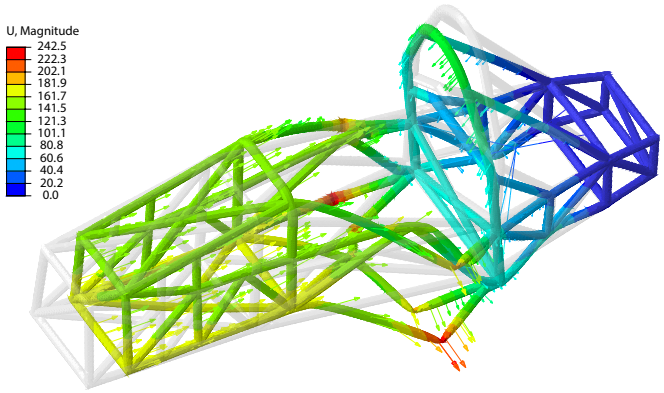

Figure 7.6: Shape of the structure (maximum deformation, at t = $3.2 \cdot 10^{-2}$ s).

7.4 Lateral impact

Regarding the lateral impact simulation, a mean acceleration of 26.1 g was obtained, which is about 5 g higher than the original composite space frame (Figure 7.7). In Figure 7.8, one can see that the maximum displacement on the side impact structure was around 107 mm, which is lower than the 114 mm of the original composite space frame. Therefore, changing from the "3-point bending case" configuration of the side impact structure, to the configuration of this chassis, with a triangulation in the middle, might be the reason for this difference. Since the lateral acceleration tolerance is around 14 g, energy-absorbing padding should be used in the sides of the driver's seat.

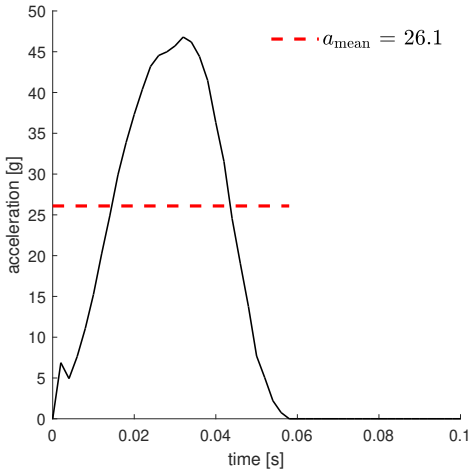

Figure 7.7: Lateral acceleration over impact time.

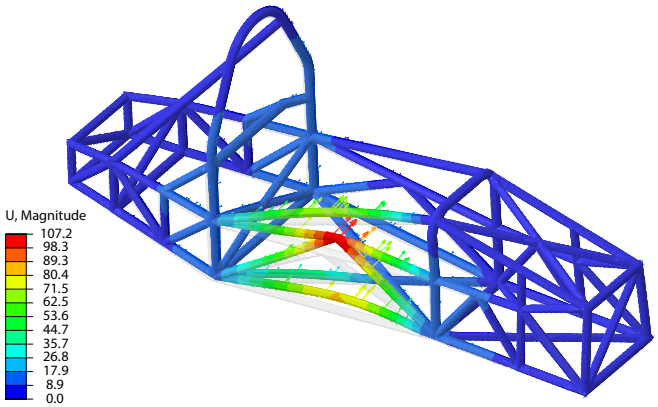

Figure 7.8: Shape of the structure after impact.

Intentionally blank page.

Chapter 8

Conclusions and recommendations

This dissertation work aimed at studying different chassis solutions for a Formula Student vehicle, at a structural level, using FEM analyses, identifying the strengths and weaknesses of each one, and the aspects to be improved. Taking the results of these analyses into consideration, the goal was to develop a new chassis, with considerable improvements compared to the previous ones.

In the first part, it was seen that there are three types of chassis used in Formula Student (space frame, monocoque and hybrid chassis), and that torsional stiffness is the main property to be taken into account when designing this type of structure. As for the materials, it was seen that carbon is the most advantageous, followed by aluminium and then steel. However, aluminium has some disadvantages, such as the welding process and cost.

Afterwards, the parameters of evaluation of the solutions under analysis were presented: weight and torsional stiffness, driver safety, ease of manufacture and cost. Hence, three types of FEM analysis were developed: static torsional test, to obtain the torsional stiffness; frontal and lateral impact simulations, to assess the driver's safety.

The composite space frame showed better results in the area associated to vehicle performance and driver safety, while the steel space frame was better in terms of ease of manufacture and materials cost. Both of them scored the same, but the composite chassis was chosen since materials cost can be mitigated with sponsorships, and it was an innovative chassis in the competition.

At the end of this work, a problem regarding the definition of the material properties of the monocoque chassis was detected. By repeating the simulations, it was concluded that this would actually be the best option to develop. The monocoque achieved great results regarding torsional stiffness, and better ones could be obtained by using core inserts, fibre reinforcements in certain areas, or another type of layup or core material. As far as the lateral impact is concerned, excellent results were obtained regarding acceleration. However, the lateral impact structure should be reinforced to reduce its deformation. Problems arose in the frontal impact simulation, so in order to complete it successfully, it would be necessary to use other mesh sizes, and to adjust the control parameters of the finite elements better.

Once the solution being developed was chosen, several aspects of the previous chassis that needed to be improved were identified. Having designed the new chassis, a quick

study to assess the impact of the placement of some tubes on torsional stiffness was performed. A selection of tube sections was also made, in such a way as to comply with the rules and minimise weight.

In the first analyses of the new chassis, there was a large increase in torsional stiffness (and specific torsional stiffness), but some problems arose in the frontal impact, due to some diagonal tubes. It was also found that in this simulation, the rigidity of the engine had to be taken into account, since the rear section of the chassis suffered large deformations.

The final solution showed significant improvements over the initial steel chassis, namely a 12.5 weight reduction and an increase in torsional stiffness of around 18 kNm/rad, resulting in 2.73kNm/(kg $\cdot$ rad) of specific stiffness. As for the crash cases, in the frontal impact scenario the structure deformed safely, and the mean acceleration was within the tolerance range. In the lateral impact, the acceleration is above the safety limit, so the use of energy-absorbing padding should be considered.

The use of carbon tubes brings some complexities that must be addressed, in order to implement the solution that was designed. Firstly, mechanical testing of the carbon tubes should be conducted, for validation of the material properties used in the FEA models. Additionally, the coupling between steel and carbon tubes, possibly by means of a structural adhesive, should be investigated, so that both functional and safety requirements are ensured.

Regarding additional FEM simulations that could be done to further improve the chassis, modal analysis is one of them. The excitation frequency, caused by the engine running, for instance, should not match a natural frequency of the system, for this will cause a resonance phenomenon. Topology optimisation could also be performed, to have a better idea of where to position some of the tubes.

Due to the unavailability of the necessary properties to fully define the damage process of the composite materials, it was only possible to reliably detect the beginning of the failures. To fully simulate the damage evolution, further simulations with a completely defined material model would be required.

In this work, it was found that the bending of the suspension arms leads to a significant loss of torsional stiffness. It is hereby recommended that the suspension department reviews the choice of these tubes. Furthermore, the geometry of the suspension, especially the attachments points of the rear one, should be revised to improve the rearmost section of the chassis, which will lead to a further weight reduction.

In brief, the goals of this dissertation work have been fulfilled, and the methods and analysis carried out here will enhance the knowledge of future team members, leading to a faster, more efficient and better design of the chassis.

References

[1] FSG, *Formula Student Rules 2020.* Formula Student Germany, 2019. Avaiable at: https://www.formulastudent.de/fsg/rules/.

[2] M. Costin and P. David, *Racing and Sports Car Chassis Design.* London: B . T. Batsford LTD, 2^{nd} ed., 1965.

[3] J. C. Brown, A. J. Robertson, and S. T. Serpento, *Motor Vehicle Structures: Concepts and Fundamentals.* Oxford: Butterworth-Heinemann, 2002.

[4] "Vehicle frame." https://en.wikipedia.org/wiki/Vehicle_frame. Last accessed: 28/02/2020.

[5] "Monocoque." https://en.wikipedia.org/wiki/Monocoque. Last accessed: 28/02/2020.

[6] C. A. Eurenius, N. Danielsson, A. Khokar, E. Krane, M. Olofsson, and J. Wass, "Analysis of Composite Chassis," Bachelor's thesis, Chalmers University of Technology, 2013.

[7] "Feature: Formula Electric Belgium Umicore LUNA." https://evodays.tech.blog/2017/01/30/feature-formula-electric-belgium-umicore-luna/. Last accessed: 28/02/2020.

[8] J. D. van Kerkhoven, "Design of a Formula Student Race Car Chassis," Master's thesis, Eindhoven University of Technology, 2008.

[9] C. Weiss, "World's first 3D-printed supercar aimed at shaking up the auto industry ." https://newatlas.com/divergent-microfactories-blade-first-3d-printed-supercar/38201/, 2015. Last accessed: 08/05/2020.

[10] "First 3D Printed Supercar - A New Way To Build Cars." https://youtu.be/O9odhgH24oA. Last accessed: 08/05/2020.

[11] W. B. Riley and A. R. George, "Design , Analysis and Testing of a Formula SAE Car Chassis," *SAE Technical Paper Series*, 2002.

[12] M. Kissai, M. Bruno, M. Xavier, D. Martinez, and A. Tapus, "Adaptive Robust Vehicle Motion Control for Future Over-Actuated Vehicles," *Machines*, pp. 1–31, 2019.

[13] C. Smith, *Tune to win: the art and science of race car development and tuning.* Fallbrook, CA: Aero Publishers, 1978.

[14] A. Deakin, D. Crolla, J. P. Ramirez, and R. Hanley, "The Effect of Chassis Stiffness on Race Car Handling Balance," in *Proceedings of the 2000 SAE Motorsports Engineering Conference & Exposition*, (Dearborn, Michigan), p. 361, SAE International, 2000.

[15] W. F. Milliken and D. L. Milliken, *Race Car Vehicle Dynamics*. Warrendale, Pa: SAE International, 1995.

[16] M. F. Ashby, *Materials Selection in Mechanical Design*. Elsevier Butterworth-Heinemann, 3rd ed., 2005.

[17] "Material property charts." https://grantadesign.com/education/students/charts/. Last accessed: 30/04/2020.

[18] E. J. Barbero, *Introduction to Composite Materials Design*. Taylor & Francis Group, 3rd ed., 2017.

[19] P. Clarke, "Pat's Columns - Space-frame Chassis." https://www.formulastudent.de/pr/news/details/article/pats-column-space-frame-chassis/, 2009. Last accessed: 04/04/2020.

[20] T. Khaled, "Preheating , Interpass and Post-Weld Heat Treatment Requirements for Welding Low Alloy Steels," Tech. Rep. October, Federal Aircraft Administration, 2014.

[21] "CDS tubing." http://teamtubellc.com/en/products/cold-drawn-seamless. Last accessed: 17/04/2020.

[22] A. Mittal, "Seamless Mechanical Steel Tubing, Specifications & Size Ranges." Avaiable at: https://tubularnorthamerica.arcelormittal.com/images/ArcelorMittal_SeamlessSpecs.pdf.

[23] Rock West Composites, "4 Methods for producing composite tubing." https://www.rockwestcomposites.com/blog/4-methods-for-producing-composite-tubing/, 2018. Last accessed: 30/04/2020.

[24] G. Gardiner, "Filament winding reinvented." https://www.compositesworld.com/articles/filament-winding-reinvented, 2018. Last accessed: 30/04/2020.

[25] N. Aldoumani, H. Haddad Khodaparast, I. Cameron, M. Friswell, D. Jones, A. Chandrashaker, and J. Sienz, "The robustness of carbon fibre members bonded to aluminium connectors in aerial delivery systems," *Cogent Engineering*, vol. 3, no. 1, pp. 1–20, 2016.

[26] "Rock West Composites webpage." https://www.rockwestcomposites.com. Last accessed: 30/04/2020.

[27] "Easy Composites webpage." https://www.easycomposites.co.uk. Last accessed: 30/04/2020.

[28] E. J. Barbero, *Finite Element Analysis of Composite Materials using Abaqus*. Taylor & Francis Group, 2013.

[29] D. Cripps, "Unidirectional Fabric." https://netcomposites.com/guide/reinforcements/unidirectional-fabric/, 2019. Last accessed: 15/05/2020.

[30] B. Wang, J. Xiong, X. Wang, L. Ma, G. Q. Zhang, L. Z. Wu, and J. C. Feng, "Energy absorption efficiency of carbon fiber reinforced polymer laminates under high velocity impact," *Materials and Design*, vol. 50, pp. 140–148, 2013.

[31] H. Singh, P. Mahajan, and K. Namala, "A progressive failure study of e-glass/epoxy composite in case of low velocity impact," in *Advances in Structural Engineering* (V. Matsagar, ed.), vol. 1, pp. 273–300, Springer India, 2015.

[32] W. D. C. Jr., *Materials Science and Engineering: an Introduction*. John Wiley & Sons, Inc., 7th ed., 2007.

[33] Euro NCAP, "Full width frontal impact testing protocol," tech. rep., Euro NCAP, Leuven, 2019.

[34] Euro NCAP, "Oblique pole side impact testing protocol," tech. rep., Euro NCAP, Leuven, 2019.

[35] "Friction and friction coefficients." https://www.engineeringtoolbox.com/friction-coefficients-d_778.html. Last accessed: 05/04/2020.

[36] "Defining plasticity in Abaqus." https://abaqus-docs.mit.edu/2017/English/SIMACAEGSARefMap/simagsa-c-matdefining.htm. Last accessed: 20/03/2020.

[37] "Material properties database." https://www.makeitfrom.com/material-properties/EN-1.0031-E190-Non-Alloy-Steel. Last accessed: 20/03/2020.

[38] M. Dewan, J. Liang, M. A. Wahab, and A. Okeil, "Effect of Post-Weld Heat Treatment and Electrolytic Plasma Processing on Tungsten Inert Gas Welded AISI- 4140 alloy steel," *Materials and Design*, vol. 54, pp. 6–13, 01 2014.

[39] R. V. Brulle, *Engineering the space age: a rocket scientist remembers*. Maxwell Air Force Base, Alabama: Air University Press, 2008.

[40] B. Riley, "Formula SAE anthropometric reference data," tech. rep., SAE International, 2015.

[41] "Damage initiation for fiber-reinforced composites." https://abaqus-docs.mit.edu/2017/English/SIMACAEMATRefMap/simamat-c-damageinitfibercomposite.htm. Last accessed: 26/04/2020.

[42] "Crushable foam plasticity models." https://abaqus-docs.mit.edu/2017/English/SIMACAEMATRefMap/simamat-c-crushfoam.htm. Last accessed: 22/05/2020.

[43] E. A. Flores-Johnson, Q. M. Li, and R. A. Mines, "Degradation of elastic modulus of progressively crushable foams in uniaxial compression," *Journal of Cellular Plastics*, vol. 44, no. 5, pp. 415–434, 2008.

[44] "Rennsport Shop webpage." https://www.rennsportshop.com. Last accessed: 03/07/2020.

[45] "Castro Composites webpage." https://www.castrocompositesshop.com. Last accessed: 03/07/2020.

Appendix A

Formula Student templates

In Figure A.1, the templates that are used to assess the size of the cockpit are shown. The template on the left must pass vertically from the cockpit opening to bellow the upper side impact member. The one on the right, should pass from the cockpit opening to a point 100 mm rearwards of the pedals [1].

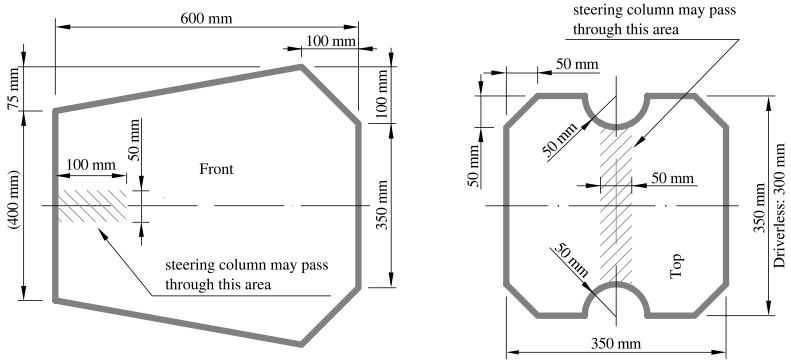

Figure A.1: Cockpit opening template (left) and cockpit internal cross section template (rigth) [1].

The 95$^{\text{th}}$ percentile male template shown in Figure A.2 should also be taken into account, since it must fit inside the cockpit.

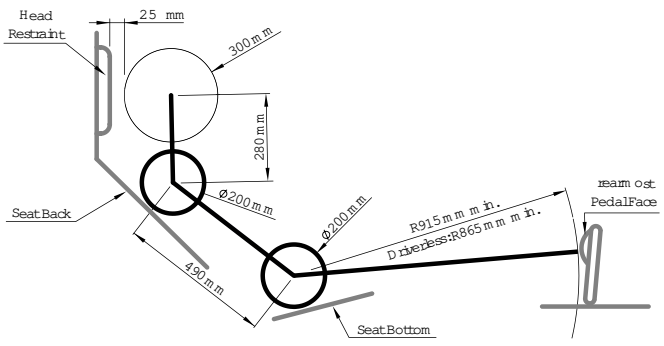

Figure A.2: 95$^{\text{th}}$ percentile male placement [1].

Intentionally blank page.

Appendix B

Concept scoring details

In Table B.1 the results of the concept scoring, for each chassis, are shown. In the following sections, the process that was used to evaluate the chassis in terms of driver safety, ease of manufacture and materials cost is explained in more detail.

Table B.1: Concept scoring of the different solutions.

Chassis type	Torsional stiffness [kNm/rad]	Mass [kg]	Driver safety	Ease of manufacture	Materials cost [€]
Steel space frame	52.27	38.4	8.0	8	465.18
Composite space frame	38.42	20.2	9.2	7	1644.42
Monocoque	51.02	18.2	7.6	4	1135.93

Scaled values

Weight / Chassis	30%	30%	20%	15%	5%	Score
Steel space frame	10	4.7	8.7	10	10	8.2
Composite space frame	6.7	9.0	10	8.8	2.8	8.2
Monocoque	9.8	10	8.2	5.0	4.1	8.5

B.1 Driver safety

The mean accelerations and the maximum displacements obtained during the FEA simulations were used to assess the driver safety Table (B.2). As it was not possible to complete the frontal impact simulations of the monocoque, the score for the frontal impact was done in a qualitative and empiric way. A score of 10 regarding acceleration

was given, the same as the composite space frame, as composite structures have good energy absorbing properties. In terms of deformation, it was rated with 5.5, as a large deformation of the structure is predicted (as it can be seen with the results obtained at the time of the simulation abortion).

Formula Student cars are required to have a frontal impact attenuator, so lateral impacts are more critical. Because of this, and also to reduce the effect of the qualitative scoring that was done, the weighting factors of the frontal acceleration and deformation was considered as 10% each.

Table B.2: Concept scoring, regarding driver safety.

Chassis type	Frontal acceleration [g]	Frontal displacement [mm]	Lateral acceleration [g]	Lateral displacement [mm]	
Steel space frame	21.1	155	22.7	166	
Composite space frame	16.8	282	21.8	114	
Monocoque	N/A	N/A	19.8	205	
		Scaled values			
Chassis \ Weight	10%	10%	40%	40%	Score
Steel space frame	8.0	10	8.7	6.9	8.7
Composite space frame	10	5.5	9.1	10	10
Monocoque	8.0	5.5	10	5.6	8.2

B.2 Ease of manufacture

Ease of manufacture was evaluated according to an estimate of the required working days, and the number of machine tools needed. For the metal space frame, the tubes should be laser cut, in order to get better quality joints, and to minimise the addition of the filling material during TIG welding.

The same applies to the composite space frame, with the additionality of having to cut the carbon tubes by hand. For both cases, the chassis production will take around 10 working days (considering that all necessary materials and machines are available).

Regarding the monocoque chassis, the process is more complex, as it requires a lot of manual labour not only to lay-up the composite fabrics and to cut and shape the core, but also to do all the mould preparation operations. For this reasons, it is expected to take around 30 days to fabricate.

B.3 Cost estimation

An estimate of the budget needed to purchase the main materials for the construction of the different chassis is shown in TableB.3. It should be noted that the filler material for the welding of the tubes in both space frame chassis, the structural adhesive to fit the tubes of the composite space frame, and the materials needed to fabricate and prepare the mould of the monocoque were not taken into account.

Table B.3: Cost estimation of the materials of the chassis.

Steel space frame

Material	Length [m]	Price [€/m]	Total cost [€]
$\varnothing_{\text{ext=}}$ 28, steel	36	10.88 [44]	465.18
$\varnothing_{\text{ext=}}$ 30, steel	6	6.28 [44]	

Composite space frame

Material	Length [m]	Price [€/m]	Total cost [€]
$\varnothing_{\text{ext=}}$ 28, steel	7.5	10.88	1644.42
$\varnothing_{\text{ext=}}$ 30, steel	6	12.25	
$\varnothing_{\text{int=}}$ 28.5, carbon	35	42.55 [27]	

Monocoque

Material	Area [m^2]	Price [€/m^2]	Total cost [€]
UD Carbon	29.7	38.03 [45]	1135.93
Rohacell foam	3.9	166.3 [27]	
	Length [m]	Price [€/m]	
$\varnothing_{\text{ext=}}$ 28, steel	6	10.88	
$\varnothing_{\text{ext=}}$ 30, steel	3	12.25	